Pressure-Temperature-Deformation-Time Constraints on the South Tibetan Detachment System in the Garhwal Himalaya (NW India)

(Article begins on next page)

07 January 2023

Pressure-temperature-deformation-time constraints on the South Tibetan Detachment System in the Garhwal Himalaya (NW India)

S. Iaccarino[1,2*], C. Montomoli[1,8], R. Carosi[2], C. Montemagni[3], H.-J. Massonne[4], A. Langone[5], A.K. Jain[6] and D. Visonà[7]

Affiliations:

[1] Dipartimento di Scienze della Terra, Università di Pisa, via S. Maria 53, 56126, Pisa, Italy.

[2] Dipartimento di Scienze della Terra, Università di Torino, via Valperga Caluso 35, 10125, Torino, Italy.

[3] Dipartimento di Scienze dell'Ambiente e della Terra, Università degli Studi di Milano - Bicocca, Piazza della Scienza 4, 20126 Milano, Italy.

[4] Institut für Mineralogie und Kristallchemie, Universität Stuttgart, Azenbergstrasse 18, 70174, Stuttgart, Germany.

[5] C.N.R., Istituto di Geoscienze e Georisorse, via Ferrata 1, 27100 Pavia, Italy.

[6] CSIR-Central Building research Institute, Roorkee-247667, India.

[7] Dipartimento di Geoscienze, Università di Padova, via Gradenigo 6, 35131 Padova, Italy.

[8] C.N.R., Istituto di Geoscienze e Georisorse, via Moruzzi 1, 56124 Pisa, Italy.

*Corresponding author: Salvatore Iaccarino (salvatore.iaccarino@dst.unipi.it).

Key Points:

- P-T-D paths and *in situ* geochronology allowed us to unravel the history of a LANF in the Higher Himalaya

- High-temperature mylonite along the South Tibetan Detachment, North India, developed after the rock experienced P ~1.0 GPa and T $\geq$ 750°C

- Ductile shearing of the STDS is constrained at ~ 20-15 Ma; brittle deformation overprinted mylonite after ~ 15 Ma

Abstract

A peculiar feature of the Himalaya is the occurrence of a system of low-angle-normal faults and shear zones, the South Tibetan Detachment System (STDS), at the mountain crests. The STDS was active during syn-convergent tectonics. We describe the STDS-related sheared rocks along the Dhauli Ganga valley, in the Garhwal Himalaya (NW India), where the Malari granite, reported as an undeformed igneous body cross-cutting the STDS, occurs. A detailed multidisciplinary study, integrating field-based, microstructural, petrographic and geochronological analyses was carried out on rocks along this valley. We demonstrate how the non-coaxial ductile portion of the STDS affected the upper part of the Greater Himalaya Sequence migmatite, which experienced peak pressure (P) – temperature (T) conditions of 0.9-1.1 GPa and $\geq$ 750°C at $\geq$ 24 Ma. This migmatite has been reworked structurally upwards leading to the formation of high-T sillimanite-bearing mylonites. Further upward, medium-T shearing deformed the Malari granite and leucogranite dykes, forming medium-T mylonites. Ductile shearing was temporally constrained, based on new *in situ* monazite datings and previously published Ar-Ar geochronology, between ~20-15 Ma. We demonstrate that a preserved ductile to brittle spatial and temporal transition of the STDS deformation exists, with the brittle features overprinting ductile ones. Our data shed new light on the geological evolution of the STDS in the NW Himalaya with implications for the relationship and relative timing of partial melting, granite emplacement and deformation along low-angle-normal faults.

1. Introduction

Normal faults with a very small dip angle (0-30°) are classified as low angle normal faults (LANFs) [*Collettini*, 2011 and references therein]. These faults are a geological puzzle since they represent an "apparent" mechanical paradox with an associated absent to moderate seismicity [*Collettini*, 2011 and references therein]. Nevertheless, they accommodate significant amounts of crustal extension. LANFs are quite common structural features in different tectonic settings. They were firstly described in the Basin and Range province of the United States of America [*Anderson*, 1971; *Wernicke*, 1981, 2009] and they were then documented in many extensional and post-orogenic settings [e.g. *Fossen et al.*, 2000; *Fossen*, 2010; *Collettini and Holdsworth*, 2004].

One of the most striking, topographically highest and best-studied cases of a LANF in an active syn-convergent tectonic regime is the South Tibetan Detachment System (STDS) in the Himalaya. This LANF was discovered and already intensively investigated in the 1980's [*Caby et al.*, 1983; *Burg et al.*, 1984; *Burchfiel and Royden*, 1985; *Burchfiel et al.*, 1992; *Hodges et al.*, 1992]. The STDS, firstly interpreted as a thrust fault [*Academia Sinica*, 1979] and later on as a normally reactivated thrust fault [*Patel et al.,* 1993; *Dèzes et al.,* 1999], is a system of top-down-to-the-N, ductile to brittle normal shear zones of variable thickness [*Carosi et al.*, 1998; *Searle* 1999, 2010; *Cottle et al.*, 2007, 2011; *Kellett et al.*, 2010, 2013; *Kellett and Grujic*, 2012; *Finch et al.,* 2014; *Shreshtha et al.*, 2015], separating medium-to-high-grade rocks of the Greater Himalayan Sequence (GHS) in the footwall, from the low- to very-low grade meta-sedimentary rocks of the Tethyan Sedimentary Sequence (TSS) in the hanging-wall. Miocene coeval top-to-the-N extensional activity along the STDS coupled with top-to-the-S contractional shearing along the Main Central Thrust (MCT) at the top and the base of the GHS, respectively, has been regarded as the main tectonic process (i.e. extrusion or channel flow), which caused the exhumation of the GHS, the metamorphic core of the

Himalaya [*Hodges et al*., 1993; *Searle*, 2010 and references therein]. During this process, the MCT and the STDS, both accommodated comparable amounts of displacement (hundreds of km). Structures and extrusion processes similar to those recognized in the Himalaya have been invoked for other active (e.g. Hellenides) or ancient (e.g. Caledonides) orogenic belts [*Grujic*, 2006 and references therein]. On the contrary, other tectonic models such as the critical taper wedge model [*Robinson et al*., 2006; *Kohn*, 2008; *Chambers et al*., 2011; *Finch et al.,* 2014] consider the STDS as a rather minor structure in the evolution of the Himalaya, with a short duration of activity and a rather small displacement (tens of km). In this framework, information on the timing of shearing, as well as the associated displacement along the STDS, is crucial.

Undeformed igneous bodies, such as the Manaslu granite in central Nepal [*Guillot et al*., 1995, but see *Searle and Godin*, 2003] or the Bura Buri granite in western Nepal [*Bertoldi et al*., 2011*; Carosi et al*., 2013], intruding the top of the GHS up to the TSS, have been commonly used to constrain the minimum age of the STDS activity [*Cottle et al*., 2015; see also *Edwards and Harrison*, 1997; *Murphy and Harrison,* 1999]. We focus in this work on the main geological features at the boundary between the upper part of the GHS and the lower portion of the TSS in the Dhauli Ganga valley (Garhwal Himalaya, NW India) because of the occurrence of a granite, the Malari leucogranite [*Sachan et al*., 2010]. The U-Pb zircon age of ~19 Ma of this igneous body, crosscutting the contact of the GHS and the TSS has also been interpreted as the age that activity ceased on the STDS [*Sachan et al*., 2010]. Combining meso- and micro-structural features and pressure-temperature-time conditions, we describe the main features and the timing of the STDS along a structural transect through the Garhwal Himalaya and clarify relationships of the STDS with the Malari granite. Our data are integrated and discussed in the context of a regional framework, with a focus on the timing of STDS-related extension along the Himalaya.

2. Geological background

2.1. The Himalayas

The Himalayan belt (Figure 1a), resulting from the collision of the Indian Plate with the southern margin of Asia in the Paleocene (57.5 Ma/59 Ma; *Jain* [2014]; *Hu et al.* [2016]), is one of the most spectacular landforms of our planet [*Hodges*, 2000]. The architecture of this orogen is characterized by an impressive lateral continuity of the main litho-tectonic units and their tectonic boundaries, for nearly 2400 km. This architecture, from N to S (Figure 1a), comprises the following: (i) the Indus-Tsangpo Suture zone (ITSZ) which is made up of ophiolitic and deep-water sediments, remnants of the Neo-Tethys basin interposed between the Indian and Asian Plates. The northward subduction of the Neo-Tethyan oceanic crust below the Asian Plate built up a volcanic arc represented by volcanic and plutonic rocks of the Transhimalaya range (Figure 1a). (ii) The TSS comprises Neo-Proterozoic/Cambrian to Eocene [*Gaetani and Garzanti*, 1991; *Sciunnach and Garzanti*, 2012] polydeformed sedimentary rocks [e.g. *Antolin et al.*, 2011; *Montomoli et al.*, 2017a] deposited on the northern part of the Indian Plate passive margin. TSS rocks generally experienced very low- to low-grade metamorphism [*Hodges*, 2000; *Dunkl et al.*, 2011] though medium-grade metamorphism is also documented at the base of the TSS, near the STDS, and in other localities [*Vannay and Hodges*, 1996; *Hodges*, 2000; *Carosi et al.*, 1998, 2014; *Searle*, 2010; *Montomoli et al.*, 2017a]. The STDS separated the TSS from the GHS in the Miocene [*Godin et al.*, 2006] and is commonly described as a composite structure of a structurally lower extensional ductile shear zone and an upper brittle normal fault [e.g. *Carosi et al.*, 1998; *Searle*, 1999]. These are represented, for instance, in the Mt. Everest region by the Lhotse and the Qomolangma detachments, respectively [*Burchfiel et al.*, 1992; *Carosi et al.*, 1998; *Searle*, 1999; *Law et al.*, 2004, 2011]. In some localities, e.g. W Nepal [*Carosi et al.*, 2002] or the Dzakaa Chu valley in Tibet [*Cottle et al.*, 2007, 2011], the STDS brittle

branch does not occur. (iii) The GHS is composed of deep-seated Late Proterozoic to Cambro-Ordovician metamorphic rocks [*Hodges*, 2000 and references therein], and is intruded by Cenozoic anatectic granite [*Visonà and Lombardo*, 2002; *Visonà et al.*, 2012] known as High Himalayan Leucogranite (HHL). In the Central Himalaya the GHS has been subdivided into three units [*Le Fort,* 1975; *Searle and Godin*, 2003; *Searle* 2010]. The lowermost one, Unit I, is composed of garnet- to kyanite-bearing metapelite and subordinated marble, calcsilicate and quartzite. Marble and calcsilicate, showing an upper amphibolite facies mineralogy [e.g. *Colchen et al.*, 1980; *Carosi et al.*, 2014; *Searle*, 2010], and minor metapelite are the main rock types of Unit II. The uppermost unit, Unit III, comprises orthogneiss, migmatite and minor marble and metapelite. This subdivision cannot be easily observed in other portions of the belt, such as NW India [e.g. *Jain et al.*, 2014] or NW Nepal [e.g. *Iaccarino et al.*, 2017 and references therein], where the amount of calcsilicate (Unit II) is rather minor. It should be stressed also that for a long time the GHS was regarded as a coherent tectonic unit, but that recent findings have challenged this view [e.g. *Montomoli et al.*, 2013, 2015; *Carosi et al.*, 2010, 2016a].

The metamorphic history of the GHS has been commonly subdivided into two main stages [e.g. *Vannay and Hodges*, 1996]. The Eo-Himalyan stage, with an Eocene-Oligocene age [*Hodges et al.*, 1994; *Vannay and Hodges*, 1996*; Carosi et al.*, 2010, 2015*; Iaccarino et al.*, 2015], is characterized by high-pressure kyanite-bearing assemblages, which were overprinted by low-pressure sillimanite- to cordierite-bearing assemblages associated with STDS-related decompression-melting of the Neo-Himalayan stage in the Miocene [*Hodges et al.*, 1994; *Hodges*, 2000]. A regime of non-coaxial deformation, with a strong component of pure shear, is commonly observed within the GHS [e.g. *Jessup et al.*, 2006; *Carosi et al.*, 2006; *Long et al.,* 2011], whereas a strong increase in the contribution of simple shear is recorded approaching the STDS [*Law et al.*, 2004; 2011] and the MCT [*Law et al.*, 2013].

(iv) The Lesser Himalayan Sequence (LHS), in the footwall of the MCT, is made up of Paleoproterozoic low- to medium-grade metamorphic rocks [*Hodges*, 2000]. The LHS is tectonically carried above the Neogene sediments of (v) the Sub-Himalaya, by the Main Boundary Thrust (MBT, Figure 1a) which was active after the Pliocene [*Hodges*, 2000].

2.2. Geology along the Alaknanda – Dhauli Ganga valleys

The study area is located in the Garhwal Himalaya (Figure 1a), NW India, along the Alaknanda-Dauli Ganga valleys (Figure 1b), where a complete structural transect of the Himalaya is exposed [*Hodges and Silverberg*, 1988; *Gururajan and Choudhuri,* 1999; *Spencer et al*., 2012a,b; *Jain et al*., 2013, 2014; *Shreshtha et al*., 2015; *Thakur et al*., 2015]. According to *Jain et al*. [2014] the general architecture of the study valleys could be simplified as N-NE dipping imbrications of rock packages with the main tectonic foliation trending NW-SE and dipping gently towards the NE. The LHS, present in the SW portion of the area (Figure 1b), is composed of garnet-bearing metapelite, limestone, quartzite, calcsilicate and amphibolite layers [*Ahmad et al.,* 2000; *Spencer et al*., 2012b; *Jain et al*., 2014]. Their metamorphic peak temperature never exceeded 480-520°C [*Célérier et al.,* 2009]. Structurally upwards, the MCT zone (MCTz in Figure 1b) comprises a sequence of highly imbricated and mylonitized rocks mainly composed of garnet-bearing paragneiss, quartzite and orthogneiss of Paleoproterozoic protolith age [*Spencer et al*., 2012a]. According to *Valdiya et al*. [1999] the MCTz is marked by two top-to-the-S shear zones: the Munsiari Thrust (MT, Figure 1b) in the lower parts and the Vaikrita Thrust (VT, Figure 1b) in the structurally upper parts. According to *Spencer et al*. [2012b] and *Thakur et al*. [2015] pressure-temperature (P-T) estimates for the MCTz are in the range of 500-600°C and 0.5-1.2

GPa, with a general structurally upward increase of P-T conditions. *Montemagni et al.* [2016] reported evidence of aqueous fluid circulation during the first stages of the MT activity.

Above the VT (Figure 1b), the GHS (the Vaikrita group, *Jain et al.,* [2014]) has been subdivided into three main formations: the structurally lower Joshimath Formation consists of kyanite+garnet+biotite+white mica±staurolite gneiss. In the middle of the GHS, kyanite+garnet± K-feldspar ±white mica gneiss, migmatitic gneiss and minor amphibolite form the Suraithota Formation. The Bhapkund Formation, at the top of the GHS, is composed of garnet+K-feldspar+sillimanite migmatite (stromatite and minor diatexite) and small tourmaline-bearing leucogranite lenses. Five different types of leucosomes/melt patches have been described by *Jain et al.* [2013] from the migmatite, reflecting different stages of structurally-controlled melting and melt migration in the Bhapkund Formation. P-T data by *Spencer et al.* [2012b] suggest an increase of P-T conditions from the Joshimath (~700-800 °C, 1.0-1.4 GPa) to the Suraithota (~800-860 °C, ~1.40 GPa) Formations, whereas similar T for the Suraithota Formation, but lower equilibration P (~0.85-1.00 GPa) were reported for the Bhapkund Formation [*Spencer et al.*, 2012b]. The P-T estimates by the latter authors are significantly higher than those reported by *Hodges and Silverberg* [1988] for the GHS rocks along the Alaknanda-Dauli Ganga valleys (530-680°C; 0.30-1.00 GPa). At the top of the Bhapkund Formation, *Jain et al.* [2014] reported evidence of top-to-the-NE extensional shearing related to ductile deformation along the STDS. Structurally above the Bhapkund Formation (Figures 1b and 1c) the TSS occurs, composed of the Neoproterozoic-Cambrian low-grade Martoli Formation and very low-grade to unmetamorphosed Post-Martoli Formation [*Jain et al.*, 2014 and references therein]. Based on white mica geochronology, the metamorphism of the TSS in the study area is as old as ~40 Ma [*Crouzet et al.*, 2007 and references therein]. Near the Malari village (Figures 1b and c) the Malari leucogranite, with an intrusion age of ~19 Ma, occurs [*Sachan et al.*, 2010; *Jain et al.*, 2014]. This granite is

composed of quartz (30%–35%), K-feldspar (35%–40%), plagioclase (15%–25%), muscovite (~5%) and tourmaline (~5%) [*Sachan et al.* 2010]. According to *Sachan et al.* [2010], this granite has intrusive contacts with both the underlying Bhapkund Formation (GHS) and the overlying Martoli Formation (TSS) on the footwall and the hanging-wall of the STDS, respectively (Figure 1c) and shows little evidence for ductile strain. Thus, this granite is an important temporal marker for the STDS activity in the NW Himalaya. This interpretation has been challenged by *Jain et al.* [2014] and *Sen et al.* [2015]. Based on detailed meso- and microstructural investigations, *Jain et al.* [2014] demonstrated that extensional deformation is widespread in the whole upper part of the GHS, including the Malari granite and the leucogranitic dykes, and referred to this structural portion of the study area as the "Dominant Extensional Zone" (see also *Shreshtha et al.* [2015]). In an attempt to understand this peculiar settings, in the following parts we describe the main meso- and micro-structural features and the metamorphic/deformational conditions in detail along a roughly SW-NE structural transect along the road to Malari village (Figure 1c).

3. Meso- and micro-structural observations

According to our field and microstructural observations, the geology around Malari has been subdivided into three main structural domains described below from the base to the top of the structural transect.

3.1. Upper GHS and high-temperature (HT) mylonites

Stromatic migmatite predominates in the upper part of the GHS, below the TSS (Figures 1c and 2). The peak-T paragenesis in this rock is biotite-garnet-aluminosilicate-quartz-plagioclase-K-feldspar (and former melt) with apatite, monazite, zircon and graphite as accessories, suggesting a likely equilibration beyond white mica stability [e.g. *Spear et al.*,

1999]. Minor white mica retrograde after aluminosilicate is present (Figure 2d). Relict

kyanite (Figure 2d) is wrapped by sillimanite. The latter forms a fabric but has no evidence of

deformation (e.g. microboudinage). This supports our interpretation that it was a syn-

kinematic mineral. Sillimanite, reddish biotite, quartz and feldspar with shape-preferred

orientation (SPO) define the main spaced schistosity, which strikes NW-SE and dips 50 to

10° NE. Object lineation, sensu *Piazolo and Passchier* [2002], trends NE-SW and E-W and

plunges 25-35° to the NE and E. In the outcrops, two structurally different leucocratic layers

(i.e. leucosomes) are present (Figures 2a, 2b and 2c). The first one is oriented parallel to the

main foliation, whereas the second one is oriented at moderate angle (20-30°) to the first one,

forming sillimanite-bearing shear bands [*Roper*, 1972]. Field observations, such as rotation of

the foliation toward parallelism with the shear zones, offset of pre-existing markers and

minor drag folds, point out the coexistence of top-down-to the SW and top-down-to the NE

shear bands (Figures 2a, 2b and 2c). No unambiguous cross-cutting relationships between the

two sets of shear bands have been found (Figures 2a, 2b and 2c). Microscopic observations

reveal that these shear bands are defined by the same sillimanite-biotite-bearing mineralogy

(Figure 2d) supporting the inference that both types of shear bands are coeval.

Structurally upward, just ≤ 2 km S of Malari, migmatitic gneiss is strongly sheared

and its fabric is reworked, with the development of high-temperature (HT) top-to-the-NE

mylonites (Figures 2e, 2f and 2g). Pegmatitic dykes, a few decimeter thick and oriented at

high angle to the mylonitic foliation, were deformed at subsolidus conditions as indicated by

stretched feldspar and quartz (Figure 2g). In a few instances dykes also appear to be

undeformed. Stretched quartz-feldspar pods (former leucosome), porphyroclasts and

deflection of the foliation around dyke walls point to a normal top-to-the-NE sense of shear

(Figures 2e and 2f). However, in a few circumstances, porphyroclasts also suggest a top-to-

the-SW sense of shear (Figure 2e).

Three mineral assemblages were microscopically identified in HT-mylonites (Figure 3). A pre-mylonitic stage, M1, is characterized by coexisting kyanite-biotite-garnet-K-feldspar-plagioclase-quartz, minor rutile and former melt. M2 is a syn-mylonitic stage, represented by syn-kinematic growth of sillimanite (after M1 kyanite, Figure 3b), biotite, and ilmenite and dynamic recrystallization of feldspar and quartz, possibly in the presence of melt (at least in the beginning). Evidence of the late retrograde stage (M3) is rare and heterogeneously distributed and is defined by the greenschist-facies mineral chlorite, white mica and albite. These minerals frequently envelop garnet and aluminosilicate. According to the assemblages described above, and further supported by thermodynamic calculations (see below), melt was likely formed during the M1 stage, but was still present during the early M2 stage. The main mylonitic foliation, classified as disjunctive anastomosing schistosity, wraps around K-feldspar, garnet and kyanite porphyroclasts. These porphyroclasts indicate a top-to-the-NE sense of shear (Figures 2f and 3a). Microscopic observations (Figures 3a-f) reveal evidence of dynamic recrystallization of feldspar and quartz. Quartz shows lobate grain boundaries and chessboard extinction patterns (Figure 3c), which are typical of the Grain Boundary Migration (GMB) deformation regime GBM$_{II}$ as defined by *Stipp et al*. [2002a, b] and *Law* [2014]. Myrmekite in K-feldspar, sometimes asymmetric, is common (Figure 3d).

Such microstructures suggest a HT ($\geq 650°C$) deformation regime during the top-to-the-NE normal (STDS-related) shearing [*Passchier and Trouw*, 2005], and are in agreement with the syn-kinematic growth of sillimanite and reddish biotite. However, despite the strong deformation, in some low-strain domains euhedral faces of feldspar (Figure 3e), interpreted as melt-precipitated [*Vernon*, 2011], are still preserved. Finally, rare veinlets, filled by quartz and feldspar (Figure 3f), crosscut the foliation. Due to the microstructural and petrological

relationships described above, HT-mylonites were chosen for a detailed study, since they might yield unique insight into P-T-t evolution of the STDS-related ductile shearing (see below).

3.2. Malari granite and medium-temperature mylonites

Close to Malari, structurally above the HT-mylonite, the small Malari granite crops out (Figure 1c). The main body is a medium- to coarse-grained intrusion, sometimes cut by leucocratic aplitic or pegmatitic bodies. Field evidence suggests that the whole Malari granite and the leucogranitic dykes are deformed and foliated (Figure 4). Ductile deformation with the development of S-C fabric and rotated feldspar porphyroclasts (Figure 4b), pointing to a top-to-the-N/NE sense of shear, are common. A system of low-angle and conjugate high-angle brittle faults (Figure 4a, see also *Jain et al*. [2014]), with associated cataclasite (Figure 4c) overprinting the mylonitic deformation, has been recognized. Where markers, such as aplitic/pegmatitic sheared bodies, were observed the fault offset never exceeded 5-10 m. Microscopic observations confirm that a mylonitic deformation affected the Malari leucogranite characterized by an anastomosing mylonitic foliation defined by micas and SPO of quartz and feldspar. Quartz shows rotated and flattened grains with undulose extinction (Figures 4d and 4e) surrounded by new grains, suggesting a regime of subgrain rotation Recrystallization (SGR: *Stipp et al*. [2002a, b]; *Law* [2014]). In a few instances, quartz shows also deformation lamellae typical of low-temperature deformation (*Stipp et al*. [2002a, b]). Both ductile and brittle structures can be observed in feldspar (Figure 4e). Ductile structures comprise undulose extinction, mechanical twinning, perthite and very rare myrmekite. Brittle features are represented by quartz-filled fractures (see also *Jain et al*., [2014]). These microstructures support a thermal deformation regime of 450-550°C close to the brittle-ductile transition of feldspar [*Passchier and Trouw,* 2005] in agreement with SGR in quartz

[*Stipp et al*., 2002a, b; *Law*, 2014]. Tourmaline is aligned along the main foliation, commonly showing boudinage (Figure 4d) with quartz fillings in necks. Finally, late transgranular fractures were observed (Figures 4d and 4e). Kinematic indicators in oriented samples, such as white mica fish, S-C-C' fabric, feldspar and tourmaline porhyroclasts with asymmetric strain shadows and domino-type feldspar porphyroclasts, confirm a top-to-the-NE sense of shear. Neither magmatic nor HT subsolidus foliation [*Paterson et al*., 1989, 1998] was discovered. It should be pointed out that despite careful field observation and sampling, coupled with microstructural analyses, undeformed sample was not found. Even samples from low strain domains show some ductile and/or brittle structures in feldspar and quartz. Hence, we suggest that the Malari granite and the leucogranitic dykes, emplaced at the interface between GHS and TSS, were affected only by subsolidus medium temperature (defined as close the brittle-ductile transition in behavior of feldspar) mylonitic shearing followed by brittle faulting during the extensional activity along the STDS.

3.3. Martoli Formation (TSS)

The base of the TSS (Figure 1c) is represented by folded quartzite, metapsammite and metapelite of the Martoli Formation. This formation still preserves sedimentary structures like bedding (S_0, Figure 4f) and cross lamination [*Spencer et al*., 2012b; *Jain et al.* 2014]. The main foliation in the Martoli Formation, related to northeast verging folds [*Spencer et al.,* 2012b], is defined by the SPO of phyllosilicates, which are mainly fine-grained white mica and chlorite (Figure 4g). Detrital large flakes of white mica were also detected (Figure 4g). Quartz displays evidence of bulging recrystallization (BLG) as revealed by small bulges between grain interfaces (Figure 4g), the small size of newgrains, and the occurrence of deformation lamellae [*Stipp et al*., 2002a, b; *Law*, 2014]. The low metamorphic peak-T ($\leq$

400°C) suggested by BLG in quartz is also supported by the observed mineralogy in the different rock types (see also *Sachan et al.* [2010]).

4 Pressure-temperature-time (P-T-t) estimates

4.1 Methods

A detailed P-T-t investigation of HT-mylonites was carried out. Oriented thin sections, cut parallel to the XZ plane of the finite strain ellipsoid, were studied. Sample GW13-62 (30°40'54.62"N, 79°53'0.16"E), a high-grade gneissic mylonite (Figures 1c and 2e), was selected for this purpose because of the sample microstructures, mineralogy and the paucity of M3 domains, that should demonstrate the conditions during the M1 and/or M2 stages.

4.1.1 P-T estimates

Mineral compositions as well as garnet X-ray compositional maps were obtained with a CAMECA SX100 electron microprobe (EMP), hosted at the Institut für Mineralogie und Kristallchemie (Universität Stuttgart), following the analytical protocol reported in *Iaccarino et al.* [2015, 2017]. This chemical information, coupled with the sequence of mineral assemblages (see above), was used to reconstruct the P-T history of the HT-mylonites applying both pseudosection modelling with PERPLE_X [*Connolly*, 2005] and THERMOCALC for the determination of an average P-T estimate [*Powell and Holland*, 1994, 2008]. Calculation procedures, as well as selected activity-compositional models, are reported in *Iaccarino et al.* [2017]. Two points deserve to be further clarified: (1) the H_2O content in the bulk composition (reported in Figure 5a) for pseudosection calculation was set to 1.75 wt%, in order to allow minor wet melting during the prograde stage. (2) THERMOCALC average P-T estimates are sensitive to the selected water activity (a_{H2O}) [*Powell and Holland*, 1994; *Mosca et al.*, 2012; *Palin et al.*, 2014]. The anatectic nature of

the selected samples likely implies an $a_{H2O} < 1$ during dehydration melting, therefore the calculation was performed with the assumption of $a_{H2O} = 0.8$.

4.1.2 U-(Th)-Pb *in situ* monazite geochronology

Monazite, a Th-bearing REE phosphate, is a powerful and versatile geochronometer [e.g. *Parrish*, 1990; *Pyle and Spear*, 2003; *Williams and Jercinovic*, 2002; 2012; *Williams et al.*, 2007; *Kohn*, 2016]. Several contributions, indeed, have shown how U-Th-Pb internal diffusion in monazite, similarly to zircon, is negligible for $T < 900°$ [e.g. *Cherniak et al.*, 2004; *Cherniak,* 2010]. Moreover, contrarily to zircon, monazite (as phosphates in general) is very resistant to metamictic process [*Harrison et al.*, 2002] and, even in strongly fluid-mediated processes, this mineral is able to preserve its original isotopic (and chemical) signature in the survived original parts of grain [*Williams et al.,* 2011]. Furthermore, *Williams and Jercinovic* [2002, 2012] among many others, have pointed out how *in situ* monazite dating, coupled with its chemical characterization, micro-structural (e.g. deformation-blastesis relationships) and petrological (e.g. sequence of main and accessories mineral growth, P-T history) analysis could give precious insights on the tectonic interpretations and on the timing of deformation and metamorphism.

For all these reasons monazite dating has already been widely used in Himalayan research [e.g. *Kohn et al.*, 2001, 2004, 2005; *Viskupic et al.*, 2005; *Cottle et al.*, 2009; *Kellett et al.*, 2010; *Carosi et al.*, 2010, 2016a; *Montomoli et al.*, 2013; *Rubatto et al.*, 2013; *Iaccarino et al.,* 2015] to constrain the tectono-metamorphic evolution of tectonites.

Textural positions and internal features of monazite from the selected sample were characterized by the aforementioned EMP. X-ray compositional maps for Y, Th, U, Ce, and Si and chemical analysis of monazite were obtained following the analytical protocol of *Iaccarino et al*. [2015]. Selected monazite grains were chosen for *in situ* geochronology.

These grains were targeted, adopting the X-ray maps as base, with a laser ablation–

inductively coupled plasma–mass spectrometer (LA-ICP-MS) hosted at Consiglio Nazionale

delle Ricerche–Istituto di Geoscienze e Georisorse in Pavia, using a spot size of 10 µm. Full

details of the instrumental and analytical procedure are reported in *Paquette and Tiepolo*

[2007] (see also *Iaccarino et al.* [2015] and *Carosi et al.* [2016a]). Data reduction was carried

out using the GLITTER® software [*van Achterbergh et al.*, 2001], whereas data processing

and plotting were done with the software ISOPLOT [*Ludwig*, 2003].

4.2 P-T-t results

4.2.1 Mineral chemistry, P-T conditions and P-T path

Selected mineral analyses of the main silicates in sample GW13-62 are reported in

Table 1. Biotite has a narrow compositional range with Mg# = $Mg/(Mg+Fe^{2+})$ in the range of

0.41-0.46, and Ti a.p.f.u. (atoms per formula unit based on 11 O) between 0.17 and 0.27.

Plagioclase is andesine with XAb = Na/(Ca+K+Na) between 0.64 and 0.70. K-feldspar is

characterized by XOr = K/(Ca+Na+K) between 0.85 and 0.96. Garnet shows "reverse"

zoning [*Tracy et al.*, 1976] as indicated by X-ray compositional maps (reported in Figure S1)

and chemical spot analyses (Table 1). Garnet cores are characterized by XFe =

$Fe/(Mg+Ca+Mn+Fe^{2+})$ (XCa, XMn and XMg are defined accordingly to XFe) between 0.68

and 0.71, XCa = 0.06-0.07, XMg = 0.16-0.17, XMn = 0.04-0.05 and Mg# = 0.16-0.20.

Garnet rims show an increase of XMn (up to 0.07-0.08) and XFe (0.73-0.75) coupled with a

decrease in XMg = 0.13-0.14, XCa = 0.04-0.06 and Mg# = 0.13-0.15. Based on this zoning it

is likely that only minimum P-T estimates can be obtained from the compositions of garnet

[*Spear*, 1991; *Spear and Florence*, 1992]. The texturally late white mica is muscovite with

Si^{4+} (a.p.f.u.) of 3.07-3.10 and XPg = Na/(Na+Ca+K) of 0.02. A P-T pseudosection was

constructed for the P-T range of 0.3-1.3 GPa and 650-900 °C (Figure 5) considering the ten-

component chemical system $Na_2O-K_2O-CaO-MnO-MgO-FeO-Al_2O_3-TiO_2-SiO_2-H_2O$

(MnNCKFMASHT). The pseudosection is dominated by four- and tri-variant fields. The observed M1 assemblage (see above) defines a triangular field (LPlKfsGrtBtKyQzRt in Figure 5a) in the P-T range of 0.85-1.30 GPa and ~750-825 °C, delimited by kyanite-out and biotite-out curves at higher temperatures and the white mica-in curve at lower temperatures (Figures 5a and 5b). Moreover, garnet core compositional isopleths of $XFe = 0.68-0.70$ and $XCa = 0.06-0.07$, and maximum observed $XAb = 0.70$ are consistent with this field, indicating a minimum P-T equilibration of the M1 assemblage around 1.0 ± 0.1 GPa and 750-775°C (Figure 5b). These findings are also in agreement with the THERMOCALC average P-T result, that indicates an equilibration at $P = 0.92 \pm 0.12$ GPa and $T = 742 \pm 42$ °C (Figure 5b). These P-T values demonstrate that the M1 equilibration was near the conditions of the HP-granulite facies [*Indares and Martignole*, 2003] at suprasolidus conditions (see also *Groppo et al*. [2010, 2012]; *Iaccarino et al*. [2017]). According to pseudosection calculation and isopleths intersections for the garnet rim composition ($XFe = 0.73-0.75$; $XCa = 0.04-0.05$), the M2 assemblage formed at ~0.60-0.70 GPa and 725-750°C and, thus, at medium P conditions of the upper amphibolite facies (Figures 5a and 5b). The M3 assemblage, due to its very local development, could not be properly modeled with the selected bulk-composition. However, the assemblage with chlorite, white mica and albite suggests greenschist-facies metamorphism [*Spear*, 1993].

On the basis of our thermodynamic calculations we suggest that the HT-mylonites experienced prograde metamorphism up to suprasolidus conditions and M1 equilibration (Figure 5b). Afterwards, these rocks were metamorphosed along a P-T path characterized by decompression and minor cooling (Figure 5b) leading to the formation of the M2 assemblage, syn-kinematic with the main normal-shearing episode (i.e. formation of HT-mylonites). A continuation of the decompression path, accompanied by significant cooling leading to local retrogression in the greenschist facies (M3) and likely fluid infiltration, is suggested.

4.2.2. Monazite texture, zoning, and U-(Th)-Pb geochronology

Monazite was detected only as matrix minerals, with grains up to 150 µm in length hosted both within biotite-dominated and quartzo-feldspathic domains. Inclusions of biotite, quartz, zircon and, in one case, white mica (Mnz4 in Figure 6) were found in monazite. Moreover, one grain rimmed by allanite was observed within a greenschist domain (M3, see above). BSE images and particularly X-ray compositional maps (Figure 6) indicate that monazite is strongly zoned, particularly in Y and Th. All analyzed grains fall in the monazite field according to the tripartite classification of *Linthout* [2007] with the introduction of U and Th in the monazite structure according to a combination of huttonite and cheralite substitutions [*Spear and Pyle*, 2002]. Monazite compositions, mainly based on Y, but also on U and Th distribution can be assigned to two main populations (Figure 6, Table 2). One population, referred to hereafter as Mnz-type-A, is related to the core of monazite and frequently constitutes the larger part of a single grain. Mnz-type-A is associated with low Y_2O_3 contents (0.14-0.80 wt%, Table 2), variable La/Gd ratios (8.3 - 16.1) and high Th and U concentrations (Figure 6, $UO_2 + ThO_2$ between 5.7 and 9.0 wt%). The aforementioned white-mica inclusion in grain Mnz4 (Figure 6) occurs in Mnz-type-A. Another population, Mnz-type-B, forms thin and often discontinuous rims and is characterized by high Y_2O_3 concentrations (1.45- 2.98 wt%) and systematically lower $UO_2 + ThO_2$ (4.75-6.25 wt%) and La/Gd ratios (5.0 - 7.0) than in Mnz-type-A. Both populations were observed in the grain rimmed by allanite. The different monazite populations were targeted for *in situ* dating directly on ordinary thin sections through LA-ICP-MS.

Isotopic results for the unknown sample and standard [Moacir, *Seydoux-Guillaume et al.*, 2002a,b] are reported in Table 3 and Table S1, respectively. Isotopic ratios of monazite from sample GW13-62 were plotted on an inverse isochron (Figure 6), the Tera-Wasserburg plot [*Tera and Wasserburg*, 1972]. This type of plot is particularly useful for young

monazite, for identifying possible age populations, the mixing of different chemical-age domains and the possible contribution of common lead [*Kohn and Vervoort*, 2008; *Cottle et al.*, 2009; *Kellett et al.*, 2010]. As commonly observed in the Himalaya [e.g. *Kohn et al.,* 2005; *Cottle et al.*, 2009; *Kellett et al.*, 2010; *Rubatto et al.*, 2013*; Iaccarino et al.*, 2015] quite a large spread of data was obtained, reflecting the chemical heterogeneity of the analyzed monazite grains (Figure 6). In particular, a systematic link between the spot location, monazite chemistry and ages, obtained with regression on the Tera-Wasserburg plot, was noted.

Mnz-type-A, often being the larger part of a grain (e.g. grain 1 and grain 6 in Table 3), yields older ages, suggesting an age-population of ~24 Ma (23.7 ± 0.64 Ma lower intercept; MSWD = 1.11; N analyses = 11). For Mnz-type-B (e.g. rims of grains 2 and 7, Table 3) an age-population around 20 Ma (20.4 ± 2.2 Ma lower intercept; MSWD = 0.79; N analyses = 3) was obtained. Some spots (n=4) located in the outer portions of the grains within Mnz-type-B domains (e.g. in the case of rims of grain 4, Table 3), but falling on the Tera-Wasserburg plot (Figure 6) between the aforementioned two age populations, are interpreted as mixing of chemical domains, which is common [e.g. *Kellett et al.*, 2010] especially considering the dimension of a laser ablation pit, the small dimensions of the high-Y rims (Mnz-type-B) and the complex 3D nature of mineral zoning.

5 Discussion

5.1 Monazite age interpretation

The close link between age and chemistry of the two different types of monazite (Mnz-type-A and Mnz-type-B) strongly supports that these two populations reflect two different stages of monazite growth/recrystallization during the P-T-deformation (D) history

[e.g. *Foster et al.*, 2002; *Foster and Parrish*, 2003; *Pyle and Spear*, 2003; *Gibson et al.*, 2004; *Langone et al.*, 2011; *Palin et al.*, 2014; *Massonne*, 2014; *Iaccarino et al.*, 2015] of the HT-mylonite (Figures 1c and 5). The behavior of monazite during metamorphism and partial melting has been extensively investigated [e.g. *Ferry*, 2000; *Kohn and Malloy*, 2004; *Janots et al.*, 2007; 2008; *Spear and Pyle*, 2002, 2010; *Spear*, 2010; *Gasser et al.*, 2012; *Rubatto et al.*, 2001, 2013; *Kelsey and Powell*, 2011; *Yakymchuk and Brown*, 2014]. These studies have shown how the distribution of chemical elements, especially Y and heavy rare earth elements (HREE), in monazite is strongly controlled by the coupled growth/dissolution of coexisting phases. Xenotime [e.g. *Pyle and Spear*, 1999; *Spear and Pyle*, 2010] and/or allanite [*Janots et al.*, 2007, 2008; *Spear*, 2010; *Tomkins and Pattison*, 2007; *Corrie and Kohn*, 2008] are the main accessories controlling the Y+HREE and Th distribution in metamorphic monazite. Indeed, common reactions introducing monazite in the assemblage during prograde metamorphism of metapelite are related to the breakdown of allanite at ~450-550 °C [*Williams et al.*, 2007; *Janots et al.*, 2007, 2008; *Kohn*, 2016], especially in relatively Ca-rich pelites [*Wing et al.*, 2003]. Garnet is regarded as the main silicate controlling the Y + HREE budget during monazite growth [e.g. *Pyle and Spear*, 1999; *Foster and Parrish*, 2003; *Kohn and Malloy*, 2004; *Spear*, 2010]. Consequently, the initial growth of monazite is expected to show higher Th and HREE+Y contents, due to the breakdown (up to the complete consumption) of allanite and/or xenotime [e.g. *Kohn et al.*, 2005]. During continuing prograde metamorphism, together with garnet growth, coexisting monazite should show low Y+HREE concentrations [e.g. *Pyle and Spear*, 1999; *Gibson et al., 2004*; *Kohn et al., 2005*; *Spear*, 2010]. During partial melting, due to the high solubility of phosphate in the peraluminous melts [e.g. *Kohn et al.*, 2005; *Spear and Pyle*, 2002, 2010], monazite dissolution is expected [*Pyle and Spear*, 2003; *Yakymchuk and Brown*, 2014], whereas during crystallization of melt by cooling, growth of monazite with high Y + HREE is expected due

to the concomitant garnet breakdown as melt crystallizes [e.g. *Gibson et al.*, 2004; *Kohn et al.*, 2005; *Yakymchuk and Brown*, 2014]. Within this framework, it is possible to interpret our monazite ages as follows [Figures 6 and 7]. The older population (Mnz-type-A) due to its low Y and higher Th contents is interpreted as a *"late prograde"* mineral, sensu *Kohn et al.* [2005], coexisting with stable garnet. Moreover, due to the finding of a white-mica inclusion in Mnz-type-A (see above), we speculate that its age of ~24 Ma predates the main melting event accompanied by white-mica breakdown. During partial melting up to the M1 event (at ~0.90-1.10 GPa, 750-775°C), monazite is expected to have been (partially) dissolved. During further decompression and minor cooling, associated with the HT-shearing and syn-kinematic formation of the M2 assemblage (~0.60-0.70 GPa, 725-750°C), retrograde [sensu *Kohn et al.*, 2005] high-Y Mnz-type-B has crystallized in the time span of 20-19 Ma. The proposed scenario is supported by pseudosection calculations [Figure 5b] showing that, from M1 (P = 1.0 GPa, T = 770°C) to M2 (P = 0.7 GPa, T = 750°C) stages, there is a decrease in the amounts of garnet (from ~11 vol% to ~5.5 vol%) and melt (from ~20 vol% to ~17 vol%). If our interpretation holds, the melting of the upper GHS is constrained between 25-24 and 20-19 Ma. The rare allanite formed at the expense of monazite under greenschist-facies conditions (M3) must be younger than 19 Ma (Figure 7). Temporarily close to the HT-shearing, at 19 ± 0.5 Ma the emplacement of the Malari granite occurred [*Sachan et al.,* 2010].

5.2 STDS evolution and pressure-temperature-deformation-time (P-T-D-t) path

Integration of these new meso- and micro-structural, metamorphic and geochronological data with those previously published allow us to constrain the history of the STDS-related ductile shearing in the study area (Figure 7). Prograde metamorphism, up to the

upper amphibolite/lower granulite facies (M1) in the upper GHS of the study area (Figures 5 and 7), lasted to ~25-24 Ma (Figure 7), as testified by Mnz-type-A ages, and potentially started in the Eocene [*Prince et al.*, 2001]. Following melting at near peak conditions (M1, Figure 7), normal non-coaxial STDS-related shearing affected the upper part of the GHS. During deformation, melt migration [*Jain et al.*, 2013; 2014] along both top-down-to-the NE and top-down -to-the SW conjugate shear bands (Figure 2) occurred [*Brown*, 1994; *Rosenberg and Handy*, 2001] supporting a general flow deformation regime (Figure 2a) with an important contribution of pure shear as commonly observed within the ductile, normally sheared upper part of the GHS [*Law et al.*, 2004; *Jessup et al.*, 2006; *Xypolias*, 2010]. A component of pure shear during the STDS-related top-to-the-N normal shearing could also explain the occurrence of few top-to-the-S porphyroclasts (see above) described in HT-mylonites [*Simpson and De Paor*, 1993; *Xypolias*, 2010]. Melt migration led to the accumulation of a silicate liquid at the GHS-TSS interface [*Weinberg*, 2016] which could have led to the emplacement of the Malari granite at ~19 ± 0.5 Ma [*Sachan et al.*, 2010]. Zr-saturation thermometry of *Sachan et al.* [2010] suggests emplacement temperatures for the Malari granite of 600-700 °C (Figure 7), in line with estimations, using Zr-saturation and Ti-in zircon thermometers, for the HHL [*Visonà and Lombardo*, 2002; *Kohn*, 2014, 2016]. Both temperature and timing overlap with P-T-t data of HT-mylonites (Figure 7), testifying that HT-normal shearing related to decompression and minor cooling was almost coeval with the Malari granite emplacement/crystallization at ~20-19 Ma, although this granite lacks any evidence of HT-shearing. Based on the structural and geochronological data presented above, we can make the following considerations. Considering the ~15 Ma white mica Ar-Ar cooling ages from the Malari granite [*Sen et al.* 2015], that are nearly 5 Ma younger than the emplacement age of the Malari granite (U-Pb zircon), and assuming "a closure temperature" for Ar in white mica of ~450 ± 50°C [*Harrison et al.*, 2009], which is close to the

deformation temperatures suggested by medium temperature-mylonite, we can infer that medium-temperature mylonitic normal shearing was confined structurally upwards with respect to the older HT-mylonite. Medium temperature shearing affected the Malari granite during the time span of <19 up to ~15 Ma (Figure 7). Both field and microstructural data indicate a spatial and temporal transition of the STDS normal-shearing towards the N/NE, from HT (~750 ± 50° C) to medium-temperature conditions (400-500 °C), comparable to the recent findings of a northwards migration of deformation in Central Nepal [*Cottle et al*. 2015].

After 15 Ma, the brittle-ductile transition at ~300 (± 50) °C [*Tullis and Yund*, 1977] for quartzo-feldspathic crust was crossed. Brittle faulting was localized in the upper part of the study transect overprinting the medium temperature-deformation within the Malari granite, probably below 0.50 GPa (Figure 7). These P-T conditions (300 ± 50°C; < 0.50 GPa) are in agreement with fluid inclusion data and chlorite-white mica thermobarometry [*Saxena et al*. 2012] on the fault-related alteration of the Malari granite. Cooling below the closure temperatures of fission track dating of zircon (~240°C, *Bernet* [2009]) and apatite (~110 °C, *Gleadow and Duddy* [1981]) occurred around 5.0 and 3.6 Ma, respectively [*Patel and Carter,* 2009]. Finally, our observations are best explained by a model in which the STDS is formed by the superimposition of younger brittle structures on ductile ones, as reported by *Kellett and Grujic* [2012].

5.3 The STDS: a glimpse to larger scale

Timing of the N-S extension along the STDS in the Himalaya has been the subject of several previous studies [e.g. *Godin et al*., 2006; *Leloup et al*., 2010; *Wang et al*., 2016]. In particular *Leloup et al*. [2010] presented a critical review of the different time constraints for the activity of the STDS (see their figure 7 and table DR7). Following the methodological approach of *Leloup et al*. [2010], we expand their analysis, integrating our findings for the

Dhauli Ganga valley (Figure 8) and those from the recent literature, in order to present an updated STDS regional picture (Figure 8). For the Zanskar region, activity of the STDS is constrained to have started at ~26-24 Ma and ceased at ~20 Ma, based on U-Pb dating of monazite in leucogranite [*Finch et al*. 2014]. For western Nepal, *Carosi et al*. [2013] reported the occurrence of an undeformed leucogranite cross-cutting the STDS at ~23-24 Ma representing the lower age limit of the activity of the STDS. Moreover, *Nagy et al*. [2015] regarded the period of 15-13 Ma as the beginning of orogen-parallel strike slip movements in this portion of the Himalaya. For Nyalam, the available geochronology led *Wang et al*. [2016] to suggest that the STDS ductile shearing occurred between 27-25 Ma and 17-15 Ma. For the Rongbuk valley near Mt. Everest (Figure 8), *Cottle et al*. [2015] reported a minimum age of the STDS-ductile shearing of 15.4 Ma, based on crystallization ages of undeformed leucogranite. However, thermochronological data of *Schultz et al*. [2017] indicate that the STDS brittle faulting lasted to ~13 Ma. For the nearby Dzakaa Chu section (Figure 8), *Cottle et al*. [2011] suggested a protracted STDS shearing between 20 and 13 Ma, according to U-(Th)-Pb titanite dating of sheared calcsilicate rocks. In the Sikkim Himalaya (Figure 8), *Kellett et al*. [2013] constrained the STDS activity between 23.6 Ma and ~13 Ma based on several geochronometers ranging from U-(Th)-Pb zircon to apatite (U-Th)/He. Data of *Kellett et al*. [2010] for north-west Bhutan (Figure 8) support a STDS ductile shearing to 15-16 Ma with the transition to brittle-ductile deformation at 13.9 Ma [*Montomoli et al*. 2017b].

The above review (Figure 8) suggests despite the fact that in several localities normal STDS shearing could have been started somewhat earlier (even as early as ~30-29 Ma; *Soucy La Roche et al*. [2016]) than previously reported, the timing of the STDS was not coeval along the entire Himalayan belt as proposed by *Godin et al*. [2006]. Indeed, in agreement with *Leloup et al*. [2010], this shearing ceased earlier in the western Himalaya compared to

the eastern Himalaya, with western Nepal as a crucial and peculiar area (Figure 8). Furthermore, in some circumstances normal shearing could be of short duration [e.g. *Finch et al.*, 2014].

Our new data on the activity of the lower ductile part of the STDS in Garhwal (20-15 Ma), in combination with the data from the Vaikrita Thrust (~ 20-15 Ma, *Carosi et al.* [2016b]) along the same transect, testify that the contemporaneous activity of the two ductile shear zones with opposite sense of shear, bounding the GHS, could be a late feature with respect to the picture proposed by *Godin et al*. [2006]. In these model, two opposite and coeval shear zones bound the GHS, leading to its extrusion in the time span of ~23-15 Ma. Recent multidisciplinary investigations in the GHS led *Carosi et al.* [2016a] to propose an *"in sequence shearing model"* where the progressive activation of ductile shear zones from the top to the bottom of the GHS started in the period 41-36 Ma with a downward migration of deformation and the progressive exhumation of different slices of the GHS. Only later, at the time of activation of the MCTz, did the entire GHS undergo exhumation and the LHS become incorporated in the frontal part of the orogenic wedge by forming duplexes at upper crustal levels. This caused a thickening of the wedge that, according to the critical taper model by *Kohn* [2008], re-equilibrated by the activation of normal shear zones and brittle faults at the top (i.e. STDS) not necessarily coeval with basal thrusting [e.g. *Chambers et al.*, 2011].

6 Conclusions

We carried out a geological investigation in order to elucidate the main features of deformation related to the STDS in the Garhwal Himalaya (NW India). This study has general implications for the relationships between LANF and leucogranite genesis and emplacement. We have demonstrated that:

1. The high-grade anatectic rocks of the upper part of the GHS experienced metamorphic conditions near the P-T range of the HP-granulite facies. Later on, these rocks were overprinted at conditions of the medium-P upper amphibolite facies.

2. The deformation due to extensional STDS-shearing is widely distributed within the upper part of the GHS up to the base of the TSS, also affecting the Malari granite. This granite and leucogranitic dykes were subjected to medium temperature ductile shear and then brittle deformation. Quartz dynamic recrystallization microstructures and metamorphic constraints underline a clear decrease of deformation temperature moving structurally from S/SW towards N/NE.

3. The STDS-related ductile-shearing is constrained to be between ~20 and 15 Ma. Afterwards, the brittle-ductile transition was crossed leading to brittle faults overprinting ductile structures. The spatial and temporal transition from HT- to medium temperature mylonite and further brittle faulting may suggests a localization of the deformation upwards and northwards.

4. A review of the timing of the activity of the STDS along the Himalaya suggests diachronicity of both the Himalayan strike and basal thrusting. This could suggest activity on the STDS occurred in pulses.

Acknowledgments

References

Academia Sinica (1979), Geological map of Lhasa-Nyalam area, Xizang (Tibet), 1:1500.000, in *A Scientific Guidebook to South Xizang (Tibet), Academia Sinica*, Beijing.

Ahmad, T., N. Harris, M. Bickle, H. Chapman, J. Bunbury, and C. Prince (2000), Isotopic constraints on the structural relationships between the Lesser Himalayan Series and the High Himalayan Crystalline Series, Garhwal Himalaya, *Geol. Soc. Am. Bull., 112*, 467–477, doi:10.1130/0016-7606(2000)112<467:ICOTSR>2.0.CO;2.

Anderson, R. E. (1971), Thin-skin distention in the Tertiary rock of southwestern Nevada, *Geol. Soc. Am. Bull., 82*, 43–58, doi:10.1130/0016-7606(1971)82[43:TSDITR]2.0.CO;2.

Antolin, B., E. Appel, C. Montomoli, I. Dunkl, L. Din, R. Gloaguen, and R. El Bay (2011), Kinematic evolution of the eastern Tethyan Himalaya: constraints from magnetic fabric and structural properties of the Triassic flysch in SE Tibet, in *Kinematic Evolution and Structural Styles of Fold-and-Thrust Belts*, edited by J. Poblet and R. Lisle, *Geol. Soc. Spec. Publ., 349*, 99–121, doi:10.1144/SP349.6.

Bernet, M. (2009), A field-based estimate of the zircon fission-track closure temperature, *Chem. Geol., 259*, 181–189, doi:10.1016/j.chemgeo.2008.10.043.

Bertoldi, L., M. Massironi, D. Visonà, R. Carosi, C. Montomoli, F. Gubert, G. Naletto, and M. G. Pelizzo (2011), Mapping the Buraburi granite in the Himalaya of Western Nepal: remote sensing analysis in a collisional belt with vegetation cover and extreme variation of topography, *Remote Sens. Environ., 115*, 1129–1144, doi:10.1016/j.rse.2010.12.016.

Brown, M. (1994), The generation, segregation, ascent and emplacement of granite magma: the migmatite-to-crustally-derived granite connection in thickened orogens, *Earth Sci. Rev., 36,* 83–130, doi:10.1016/0012-8252(94)90009-4.

Burchfiel, B. C., and L. H. Royden (1985), North-south extension within the convergent Himalayan region, *Geology, 13*, 679–682, doi:10.1130/0091-7613(1985)13<679:NEWTCH>2.0.CO;2.

Burchfiel, B. C., Z. Chen, K. V. Hodges, Y. Liu, L. H. Royden, C. Deng, and J. Xu (1992), The South Tibetan Detachment System, Himalayan Orogen. Extension contemporaneous with and parallel to shortening in a collisional mountain belt, *Geol. Soc. Am. Spec. Pap., 269*, 1–41, doi:10.1130/SPE269-p1.

Burg, J. P., M. Brunel, D. Gapais, G .M. Chen, and G. H. Liu (1984), Deformation of leucogranites of the crystalline Main Central Sheet in southern Tibet (China), *J. Struct. Geol., 6*, 535–542, doi:10.1016/0191-8141(84)90063-4.

Caby, R. A., A. Pêcher, and P. Le Fort (1983), Le grand chevauchement central himalayen: Nouvelles données sur le métamorphisme inverse à la base de la Dalle du Tibet, *Rev. Geol. Dyn. Geogr. Phys., 24*, 89–100.

Carosi, R., B. Lombardo, G. Molli, G. Musumeci, and P. C. Pertusati (1998), The south Tibetan detachment system in the Rongbuk valley, Everest region: deformation features and geological implications, *J. Asian Earth Sci., 16*, 299–311, doi:10.1016/S0743-9547(98)00014-2.

Carosi, R., C. Montomoli, and D. Visonà (2002), Is there any detachment in the Lower Dolpo (Western Nepal)?, *C. R. Geosci., 334*, 933–940, doi:10.1016/S1631-0713(02)01828-X.

Carosi, R., C. Montomoli, D. Rubatto, and D. Visonà (2006), Normal-sense shear zones in the core of the Higher Himalayan Crystallines (Bhutan Himalaya): evidence for extrusion?, in *Channel Flow, Ductile Extrusion and Exhumation in Continental Collision Zones,* edited by R. D. Law, M. P. Searle, and L. Godin, *Geol. Soc. Spec. Publ., 268,* 425–444, doi:10.1144/GSL.SP.2006.268.01.20.

Carosi, R., C. Montomoli, D. Rubatto, and D. Visonà (2010), Late Oligocene high-temperature shear zones in the core of the Higher Himalayan Crystallines (Lower Dolpo, Western Nepal), *Tectonics, 29*, TC4029, doi:10.1029/2008TC002400.

Carosi, R., C. Montomoli, D. Rubatto, and D. Visonà (2013), Leucogranite intruding the South Tibetan Detachment in western Nepal: implications for exhumation models in the Himalayas, *Terra Nova, 25*, 478–489, doi:10.1111/ter.12062.

Carosi, R., L. Gemignani, L. Godin, S. Iaccarino, K. Larson, C. Montomoli, and S. M. Rai (2014), A geological journey through the deepest gorge on Earth: the Kali Gandaki valley section, central Nepal, in *Geological field trips in the Himalaya, Karakoram and Tibet*, edited by C. Montomoli, R. Carosi, R.D. Law, S. Singh, and S. M. Rai, *J. Virtual Explorer, 47*, paper 9.

Carosi, R., C. Montomoli, A. Langone, A. Turina, B. Cesare, S. Iaccarino, L. Fascioli, D. Visonà, A. Ronchi, and S. M. Rai (2015), Eocene partial melting recorded in peritectic garnets from kyanite-gneiss, Greater Himalayan Sequence, central Nepal, in *Tectonics of the Himalaya*, edited by S. Mukherjee et al., *Geol. Soc. Spec. Publ., 412*, 111–129, doi:10.1144/SP412.1.

Carosi, R., C. Montomoli, S. Iaccarino, H. -J. Massonne, D. Rubatto, A. Langone, L. Gemignani, and D. Visonà (2016a), Middle to late Eocene exhumation of the Greater Himalayan Sequence in the Central Himalayas: Progressive accretion from the Indian plate, *Geol. Soc. Am. Bull., 128*, 1571–1592, doi:10.1130/B31471.1.

Carosi, R., C. Montomoli, S. Iaccarino, C. Montemagni, I. M. Villa, and A. K. Jain (2016b), The Main Central Thrust Zone activity in Garhwal (India, NW Himalaya): insights from geochronological and microthermometric studies, *88th Congresso Società Geologica Italiana, Napoli, Italia, Rend. Online Soc. Geol. It.*, *40*, 167.

Célérier, J., T. M. Harrison, O. Beyssac, F. Herman, W. J. Dunlap, and A. A. G. Webb (2009), The Kumaun and Garwhal Lesser Himalaya, India; Part 2. Thermal and deformation histories, *Geol. Soc. Am. Bull., 121,* 1281–1297, doi:10.1130/B26343.1.

Chambers, J., R. Parrish, T. Argles, N. Harris, and M. Horstwood (2011), A short- duration pulse of ductile normal shear on the outer South Tibetan detachment in Bhutan: alternating channel flow and critical taper mechanics of the eastern Himalaya, *Tectonics, 30*, TC2005, doi:10.1029/2010TC002784.

Cherniak, D. J. (2010), Diffusion in Accessory Minerals: Zircon, Titanite, Apatite, Monazite and Xenotime, *Rev. Mineral. Geochem.,* 72, 827–869, doi: 10.2138/rmg.2010.72.18.

Cherniak, D.J., E. B., Watson, and M. Grove (2004), Pb diffusion in monazite: a combined RBS/SIMS study, *Geochim. Cosmochim. Ac., 68,* 829–840.

Colchen, M., P. Le Fort, and A. Pêcher (1980), Carte géologique Annapurna-Manaslu-Ganesh, Hímalaya du Népal 1/200.000, *Centre National de la Recherche Scientifique*, Paris.

Collettini, C. (2011), The mechanical paradox of low-angle normal faults: current understanding and open questions, *Tectonophysics, 510*, 253–268, doi:10.1016/j.tecto.2011.07.015.

Collettini, C., and R. E. Holdsworth (2004), Fault zone weakening processes along low-angle normal faults: insights from the Zuccale Fault, Elba, Italy, *J. Geol. Soc., 161*, 1039–1051, doi:10.1144/0016-764903-179.

Connolly, J. A. D. (2005), Computation of phase equilibria by linear programming: a tool for geodynamic modeling and its application to subduction zone decarbonation, *Earth Planet. Sci. Lett., 236*, 524–541, doi:10.1016/j.epsl.2005.04.033.

Corrie, S. L., and M. J. Kohn (2008), Trace-element distributions in silicates during prograde metamorphic reactions: Implications for monazite formation, *J. Metamorph. Geol., 26*, 451–464, doi:10.1111/j.1525-1314.2008.00769.x.

Cottle, J. M., M. J. Jessup, D. L. Newell, M. P. Searle, R. D. Law, and M. S. A. Horstwood (2007), Structural insights into the early stages of exhumation along an orogen-scale detachment: The South Tibetan Detachment System, Dzakaa Chu section, Eastern Himalaya, *J. Struct. Geol., 29*, 1781–1797, doi:10.1016/j.jsg.2007.08.007.

Cottle, J. M, M. P. Searle, M. S. A. Horstwood, and D. J. Waters (2009), Timing of mid-crustal metamorphism, melting and deformation in the Mount Everest region of Southern Tibet revealed by U(–Th)–Pb geochronology, *J. Geol., 117*, 643–664, doi:10.1086/605994.

Cottle, J. M., D. J. Waters, D. Riley, O. Beyssac, and M. J. Jessup (2011), Metamorphic history of the South Tibetan Detachment System, Mt. Everest region, revealed by RSCM thermometry and phase equilibria modelling, *J. Metamorph. Geol., 29*, 561–582, doi:10.1111/j.1525-1314.2011. 00930.x.

Cottle, J. M., M. P. Searle, M. J. Jessup, J. L. Crowley, and R. D. Law (2015), Rongbuk re-visited: Geochronology of leucogranites in the footwall of the South Tibetan Detachment System, Everest Region, Southern Tibet, *Lithos, 227*, 94–106, doi:10.1016/j.lithos.2015.03.019.

Crouzet, C., I. Dunkl, L. Paudel, P. Árkai, T. M. Rainer, K. Balogh, and E. Appel (2007), Temperature and age constraints on the metamorphism of the Tethyan Himalaya in Central Nepal: a multidisciplinary approach, *J. Asian Earth Sci., 30*, 113–130, doi:10.1016/j.jseaes.2006.07.014.

Dèzes, P. J., J. -C.Vannay, A. Steck, F. Bussy, and M. Cosca (1999), Synorogenic extension: Quantitative constraints on the age and displacement of the Zanskar shear zone (northwest Himalaya), *Geol. Soc. Am. Bull., 111*, 364–374 doi:10.1130/0016-7606(1999)111<0364:SEQCOT>2.3.CO;2.

Dunkl, I., B. Antolín, K. Wemmer, G. Rantitsch, M. Kienast, C. Montomoli, L. Ding, R. Carosi, E. Appel, R. El Bay, Q. Xu, H., and von Eynatten (2011), Metamorphic evolution of the Tethyan Himalayan flysch in SE Tibet, in *Growth and Collapse of the Tibetan Plateau*, edited by R. Gloaguen, and L. Ratschbacher, *Geol. Soc. Spec. Publ., 353*, 45–69, doi:10.1144/SP353.4.

Edwards, M. A., and T. M. Harrison (1997), When did the roof collapse? Late Miocene north–south extension in the high Himalaya revealed by Th–Pb monazite dating of the Khula Kangri Granite, *Geology, 25*, 543–546, doi:10.1130/0091-7613(1997)025<0543:WDTRCL>2.3.CO;2.

Ferry, J. M. (2000), Patterns of mineral occurrence in metamorphic rocks, *Am. Mineral., 85*, 1573–1588, doi:10.2138/am-2000-11-1201.

Finch, M., P. Hasalová, R. F. Weinberg, and C. M. Fanning (2014), Switch from thrusting to normal shearing in the Zanskar shear zone, NW Himalaya: Implications for channel flow, *Geol. Soc. Am. Bull.*, *126*, 892–924, doi:10.1130/B30817.1v.

Fossen, H. (2010), Extensional tectonics in the North Atlantic Caledonides: a regional view, in *Continental Tectonics and Mountain Building: The Legacy of Peach and Horne*, edited by R.D. Law et al., *Geol. Soc. Spec. Publ., 335*, 767–793, doi:10.1144/SP335.31.

Fossen, H., T. Odinsen, R. B. Færseth, and R. H. Gabrielsen (2000), Detachments and low-angle faults in the northern North Sea rift system, in *Dynamics of the Norwegian Margin*, edited by A. Nøttved et al., *Geol. Soc. Spec. Publ., 167*, 105–131, doi:10.1144/GSL.SP.2000.167.01.06.

Foster, G., and R. R. Parrish (2003), Metamorphic monazite and the generation of P-T-t paths, in *Geochronology: Linking the Isotopic Record with Petrology and Textures*, edited by D. Vance, W. Müller and I. M. Villa, *Geol. Soc. Spec. Publ., 220*, 25–47, doi:10.1144/GSL.SP.2003.220.01.02.

Foster, G., H. D. Gibson, R. R. Parrish, M. Horstwood, J. Fraser, and A. Tindle (2002), Textural, chemical and isotopic insights into the nature and behaviour of metamorphic monazite, *Chem. Geol., 191*, 183–207, doi:10.1016/S0009-2541(02)00156-0.

Gaetani, M., and E. Garzanti (1991), Multicyclic history of the northern India continental margin (NW Himalaya), *Am. Ass. Petrol. Geol. Bull., 75,* 1427–1446.

Gasser, D., E. Bruand, D. Rubatto, and K. Stüwe (2012), The behaviour of monazite from greenschist facies phyllites to anatectic gneisses: an example from the Chugach Metamorphic Complex, southern Alaska, *Lithos, 134–135*, 108–122, doi:10.1016/j.lithos.2011.12.003.

Gibson, H. D., S. D. Carr, R. L. Brown, and M. A. Hamilton (2004), Correlations between chemical and age domains in monazite, and metamorphic reactions involving major pelitic phases: an integration of ID-TIMS and SHRIMP geochronology with Y-Th-U X-ray mapping, *Chem. Geol., 211*, 237–260, doi:10.1016/j.chemgeo.2004.06.028.

Gleadow, A. J. W., and I. R. Duddy (1981), A natural long-term track annealing experiment for apatite, *Nucl. Tracks, 5*, 169–174, doi:10.1016/0191-278X(81)90039-1.

Godin, L., D. Grujic, R. D. Law, and M. P. Searle (2006), Channel flow, ductile extrusion and exhumation in continental collision zones: an introduction, in *Channel Flow, Ductile Extrusion and Exhumation in Continental Collision Zones,* edited by R. D. Law, M. P. Searle, and L. Godin, *Geol. Soc. Spec. Publ., 268*, 1–23, doi:10.1144/GSL.SP.2006.268.01.01.

Groppo, C., F. Rolfo, and A. Indares (2012), Partial melting in the Higher Himalayan Crystallines of Eastern Nepal: the effect of decompression and implications for the 'Channel Flow' model, *J. Petrol., 53*, 1057–1088, doi:10.1093/petrology/egs009.

Groppo, C., D. Rubatto, F. Rolfo, and B. Lombardo (2010), Early Oligocene partial melting in Main Central Thrust Zone (Arun valley, eastern Nepal Himalaya), *Lithos, 118*, 287–301, doi:10.1016/j.lithos.2010.05.003.

Grujic, D. (2006), Channel flow and continental collision tectonics: an overview, in *Channel Flow, Ductile Extrusion and Exhumation in Continental Collision Zones,* edited by R. D. Law, M. P. Searle, and L. Godin, *Geol. Soc. Spec. Publ., 268*, 25–37, doi:10.1144/GSL.SP.2006.268.01.02.

Guillot, S., P. Le Fort, A. Pêcher, M. R. Barman, and J. Aprahamian (1995), Contact metamorphism and depth of emplacement of the Manaslu granite (central Nepal). Implications for Himalayan orogenesis, *Tectonophysics, 241*, 99–119, doi:10.1016/0040-1951(94)00144-X.

Gururajan, N. S., and B. K. Choudhuri (1999), Ductile Thrusting, metamorphism and Normal faulting in Dhauliganga Valley, Garhwal Himalaya, *Himalayan Geol., 20*, 19–29.

Harrison, T. M., E. J. Catlos, and J. M. Montel (2002), U-Th-Pb dating of phosphates, *Rev. Mineral. Geochem., 48,* 523–558.

Harrison, T. M., J. Célérier, A. B. Aikman, J. Hermann, and M. T. Heizler (2009), Diffusion of ^{40}Ar in muscovite, *Geoch. Cosmochim. Acta*, *73*, 1039–1051, doi:10.1016/j.gca.2008.09.038.

Herron, M. M. (1988), Geochemical classification of terrigenous sands and shales from core or log data, *J. Sediment. Res.*, *58*, 820–829.

Hodges, K. V. (2000), Tectonics of the Himalaya and southern Tibet from two perspectives, *Geol. Soc. Am. Bull., 112,* 324–350. doi:10.1130/0016-7606(2000)1.

Hodges, K. V., and D. S. Silverberg (1988), Thermal evolution of the Greater Himalaya, Garhwal, India, *Tectonics, 7*, 583–600, doi:10.1029/TC007i003p00583.

Hodges, K. V., R. R. Parrish, T. B. Housh, D. R. Lux, B. C. Burchfiel, L.H . Royden, and Z. Chen (1992), Simultaneous Miocene extension and shortening in the Himalayan orogen, *Science, 258*, 1466–1470, doi:10.1126/science.258.5087.1466.

Hodges, K. V., B. C. Burchfiel, L. H. Royden, Z. Chen, and Y. Liu (1993), The metamorphic signature of contemporaneous extension and shortening in the central Himalayan orogen: data from the Nyalam transect, southern Tibet, *J. Metamorph. Geol., 11,* 721–737. doi:10.1111/j.1525-1314.1993.tb00183.x.

Hodges, K. V., W. E. Eames, W. Olszewski, B. C. Burchfiel, L. H. Royden, and Z. Chen (1994), Thermobarometric and ^{40}Ar/^{39}Ar geochronologic constraints on Eohimalayan metamorphism in the Dinggyê area, southern Tibet, *Contrib. Mineral. Petrol., 117*, 151–163, doi:10.1007/BF00286839.

Holdaway, M. J. (1971), Stability of andalusite and the aluminum silicate phase diagram, *Am. J. Sci.*, *271*, 97–131, doi:10.2475/ajs.271.2.97.

Hu, X., E. Garzanti, J. Wang, W. Huang, W. An, and A. Webb (2016), The timing of India-Asia collision onset – Facts, theories, controversies, *Earth-Sci. Rev., 160*, 264–299, doi:10.1016/j.earscirev.2016.07.014.

Iaccarino, S., C. Montomoli, R. Carosi, H. -J. Massonne, A. Langone, and D. Visonà (2015), Pressure–temperature–time–deformation path of kyanite-bearing migmatitic paragneiss in the Kali Gandaki valley (Central Nepal): Investigation of Late Eocene–

Early Oligocene melting processes, *Lithos, 231*, 103–121, doi:10.1016/j.lithos.2015.06.005.

Iaccarino, S., C. Montomoli, R. Carosi, H. -J. Massonne, and D. Visonà (2017), Geology and tectono-metamorphic evolution of the Himalayan metamorphic core: insights from the Mugu Karnali transect, Western Nepal (Central Himalaya), *J. Metamorph. Geol*., *35*, 301–325, doi:10.1111/jmg.12233.

Indares, A. D., and J. Martignole (2003), Towards the upper limits of the granulite facies, *J. Metamorph. Geol., 21*, 1–2, doi:10.1046/j.1525-1314.2003.00426.x.

Jain, A. K. (2014), When did India–Asia collide and make the Himalaya? *Current Sci., 106 (2)*, 254–266.

Jain, A. K., P. Seth, M. Shreshtha, P. K. Mukherjee, and K. Singh (2013), Structurally-controlled melt accumulation: Himalayan migmatites and related deformation, Dhauli Ganga Valley, Garhwal Himalaya, *J. Geol. Soc. India, 82*, 313–318, doi:10.1007/s12594-013-0158-8.

Jain, A. K., M. Shreshtha, P. Seth, L. Kanyal, R. Carosi, C. Montomoli, S. Iaccarino, and P. K. Mukherjee (2014), The Higher Himalayan Crystallines, Alaknanda – Dhauli Ganga Valleys, Garhwal Himalaya, India, in *Geological field trips in the Himalaya, Karakoram and Tibet*, edited by C. Montomoli, R. Carosi, R.D. Law, S. Singh, and S. M. Rai, *J. Virtual Explorer, 47*, paper 8.

Janots, E., F. Brunet, B. Goffè, C. Poinssot, M. Burchard, and L. Cemic (2007), Thermochemistry of monazite-(La) and dissakisite-(La): implications for monazite and allanite stability in metapelites, *Contrib. Mineral. Petrol., 154*, 1–14, doi:10.1007/s00410-006-0176-2.

Janots, E., M. Engi, A. Berger, J. Allaz, J. O. Schwarz, and C. Spandler (2008), Prograde metamorphic sequence of REE minerals in pelitic rocks of the Central Alps: implications for allanite–monazite–xenotime phase relations from 250 to 610°C, *J. Metamorph. Geol.*, *26*, 509–526, doi:10.1111/j.1525-1314.2008.00774.x.

Jessup, M. J., R. D. Law, M. P. Searle, and M. S. Hubbard (2006), Structural evolution and vorticity of flow during extrusion and exhumation of the Greater Himalayan Slab, Mount Everest Massif, Tibet/Nepal: Implications for orogen-scale flow partitioning, in *Channel Flows, Ductile Extrusion and Exhumation in Continental Collision Zones*, edited by R.D. Law, M.P. Searle and L. Godin, *Geol. Soc. Spec. Publ., 268*, 379–413, doi:10.1144/GSL.SP.2006.268.01.18.

Kellett, D. A., D. Grujic, C. Warren, J. Cottle, R. Jamieson, and T. Tenzin (2010), Metamorphic history of a syn-convergent orogen-parallel detachment: The South Tibetan detachment system, Bhutan Himalaya, *J. Metamorph. Geol., 28*, 785–808, doi: 10.1111/j.1525-1314.2010.00893.x.

Kellett, D. A., and D. Grujic (2012), New insight into the South Tibetan detachment system: not a single progressive deformation, *Tectonics, 31*, TC2007, doi:10.1029/2011TC002957.

Kellett, D. A., I. Coutand, J. Cottle, and M. Mukul (2013), The South Tibetan detachment system facilitates ultra rapid cooling of granulite-facies rocks in Sikkim Himalaya, *Tectonics, 32*, 252–270, doi:10.1002/tect.20014.

Kelsey, D. E., and R. Powell (2011), Progress in linking accessory mineral growth and breakdown to major mineral evolution in metamorphic rocks: a thermodynamic

approach in the Na_2O-CaO-K_2O-FeO-MgO-Al_2O_3-SiO_2-H_2O-TiO_2-ZrO_2 system, *J. Metamorph. Geol., 29*, 151–166, doi:10.1111/j.1525-1314.2010.00910.x.

Kohn, M. J. (2008), P- T- t data from central Nepal support critical taper and repudiate large channel flow of the Greater Himalayan Sequence, *Geol. Soc. Am. Bull., 120*, 259–273, doi:10.1130/B26252.1.

Kohn, M. J. (2014), Himalayan Metamorphism and its Tectonic Implications, *Annu. Rev. Earth Pl. Sci., 42*, 381–419, doi:10.1146/annurev-earth-060313-055005.

Kohn, M. J. (2016), Metamorphic chronology, a tool for all ages: past achievements and future prospects, *Am. Mineral., 101*, 25–42, doi:10.2138/am-2016-5146.

Kohn, M. J., E. J. Catlos, F. J. Ryerson, and T. M. Harrison (2001), Pressure–temperature– time path discontinuity in the Main Central thrust zone, central Nepal, *Geology, 29,* 571–574, doi:10.1130/0091-7613(2001)029<0571:PTTPDI>2.0.CO;2.

Kohn, M. J., M. Wielnand, C. D. Parkinson, and B. N. Upreti (2004), Miocene faulting at plate tectonic velocity in the Himalaya of central Nepal, *Earth Planet. Sci. Lett., 228*, 299–310, doi:10.1016/j.epsl.2004.10.007.

Kohn, M. J., M. Wielnand, C. D. Parkinson, and B. N. Upreti (2005), Five generation of monazite in Langtang gneisses: implication for chronology of the Himalayan metamorphic core, *J. Metamorph. Geol., 23*, 399–406, doi:10.1111/j.1525-1314.2005.00584.x.

Kohn, M. J., and M. A. Malloy (2004), Formation of monazite via prograde metamorphic reactions among common silicates: implications for age determination, *Geochim. Cosmochim. Ac., 68*, 101–113, doi:10.1016/S0016–7037(03)00258-8.

Kohn, M. J., and J. D. Vervoort (2008), U- Th- Pb dating of monazite by single- collector ICP- MS: Pitfalls and potential, *Geochem., Geophys., Geosyst., 9*, Q04031, doi:10.1029/2007GC001899.

Langone, A., R. Braga, H. -J. Massonne, and M. Tiepolo (2011), Preservation of old (prograde metamorphic) U–Th–Pb ages in unshielded monazite from high-pressure paragneiss of the Variscan Ulten Zone, *Lithos, 127*, 68–85, doi:10.1016/j.lithos.2011.08.007.

Law, R. D. (2014), Deformation thermometry based on quartz c-axis fabric and recrystallization microstructures: a review, *J. Struct. Geol., 66*, 129–161, doi:10.1016/j.jsg.2014.05.023.

Law, R. D., M. P. Searle, and R. L. Simpson (2004), Strain, deformation temperatures and vorticity of flow at the top of the Greater Himalayan Slab, Everest Massif, Tibet, *J. Geol. Soc., 161*, 305–320, doi:10.1144/0016-764903-047.

Law, R. D., M. J. Jessup, M. P. Searle, M. Francis, D. Waters, and J. M. Cottle (2011), Telescoping of isotherms beneath the South Tibetan Detachment System, Mount Everest Massif, *J. Struct. Geol., 33*, 1569–1594, doi:10.1016/j.jsg.2011.09.004.

Law, R. D., D. W. Stahr, M. K. Francsis, K. T. Ashley, B. Grasemann, and T. Ahmad (2013), Deformation temperatures and flow vorticities near the base of the Greater Himalayan Series, Sutlej Valley and Shimla Klippe, NW India, *J. Struct. Geol., 54*, 21–53 doi:10.1016/j.jsg.2013.05.009.

Le Fort, P. (1975), Himalaya: the collided range: present knowledge of the continental arc, *Am. J. Sc., 275*, 1–44.

Leloup, P. H., G. Mahéo, N. Arnaud, E. Kali, E. Boutonnet, D. Liu, X. Liu, and L. Haibing (2010), The South Tibet detachment shear zone in the Dinggye area. Time constraints on extrusion models of the Himalayas, *Earth Planet. Sci. Lett., 292*, 1–16, doi:10.1016/j.epsl.2009.12.035.

Linthout, K. (2007), Tripartite division of the system $2REEPO_4 - CaTh(PO_4)_2 - 2ThSiO_4$, discreditation of brabantite, and recognition of cheralite as the name for members dominated by $CaTh(PO_4)_2$, *Can. Mineral., 45*, 243–248, doi:10.2113/gscanmin.45.3.503.

Long S., N. McQuarrie, T. Tobgay, and J. Hawthorne (2011), Quantifying internal strain and deformation temperature in the eastern Himalaya, Bhutan: Implications for the evolution of strain in thrust sheets, *J. Struct. Geol., 33*, 579–608, doi.org/10.1016/j.jsg.2010.12.011.

Ludwig, K. R. (2003), Isoplot/Ex version 3.0. A geochronological toolkit for Microsoft Excel, *Spec. Publ., 4,* Geochronol. Cent., Berkeley, Calif.

Massonne, H. -J. (2014), Wealth of P–T–t information in medium-high grade metapelites: example from the Jubrique Unit of the Betic Cordillera, S Spain, *Lithos, 208-209*, 137–157, doi:10.1016/j.lithos.2014.08.027.

Montemagni, C., P. Fulignati, S. Iaccarino, P. Marianelli, C. Montomoli, and A. Sbrana (2016), Deformation and fluid flow in the Munsiari Thrust (NW India): a preliminary fluid inclusion study, *Atti Soc. Tosc. Sci. Nat.*, doi:10.2424/ASTSN.M.2016.22.

Montomoli, C., S. Iaccarino, R. Carosi, A. Langone, and D. Visonà (2013), Tectonometamorphic discontinuities within the Greater Himalayan Sequence in Western Nepal (Central Himalaya): Insights on the exhumation of crystalline rocks, *Tectonophysics, 608*, 1349–1370, doi:10.1016/j.tecto.2013.06.006.

Montomoli, C., R. Carosi, and S. Iaccarino (2015), Tectonometamorphic discontinuities in the Greater Himalayan Sequence: a local or a regional feature?, in *Tectonics of the Himalaya*, edited by S. Mukherjee et al., *Geol. Soc. Spec. Publ., 412*, 21–41, doi:10.1144/SP412.3.

Montomoli, C., S. Iaccarino, B. Antolin, E. Apple, R. Carosi, I. Dunkl, L. Ding, and D. Visonà (2017a), Tectono-metamorphic evolution of the Tethyan Sedimentary Sequence (Himalayas, SE Tibet). *It. J. Geosci., 136*, 73–88, doi:10.3301/IJG.2015.42.

Montomoli, C., R. Carosi, D. Rubatto, D. Visonà and S. Iaccarino (2017b), Tectonic activity along the inner margin of the South Tibetan Detachment constrained by syntectonic leucogranite emplacement in Western Bhutan. *It. J. Geosci., 136*, 5–14, doi:10.3301/IJG.2015.26.

Mosca, P., C. Groppo, and F. Rolfo (2012), Structural and metamorphic features of the Main Central Thrust Zone and its contiguous domains in the eastern Nepalese Himalaya, *J. Virtual Explorer, 41*, paper 2, doi:10.3809/jvirtex.2011.00294.

Murphy, M. A., and T. M. Harrison (1999), Relationship between leucogranites and the Qomolangma detachment in the Rongbuk Valley, south Tibet, *Geology, 27*, 831–834, doi:10.1130/0091-7613(1999)027<0831:RBLATQ>2.3.CO;2

Nagy, C., L. Godin, B. Antolín, J. Cottle, and D. Archibald (2015), Mid-Miocene initiation of orogen-parallel extension, NW Nepal Himalaya, *Lithosphere, 7*, 483–502, doi:10.1130/L425.1.

Palin, R. M., M. P. Searle, M. R. St-Onge, D. J. Waters, N. M. W. Roberts, M. S. A. Horstwood, R. R. Parrish, O. M. Weller, S. Chen, and J. Yang (2014), Monazite geochronology and petrology of kyanite- and sillimanite-grade migmatites from the northwestern flank of the eastern Himalayan syntaxis, *Gondwana Res., 26*, 323–347, doi:10.1016/j.gr.2013.06.022.

Paquette, J. L., and M. Tiepolo (2007), High resolution (5 μm) U–Th–Pb isotope dating of monazite with excimer laser ablation (ELA)-ICPMS, *Chem. Geol., 240*, 222–237, doi:10.1016/j.chemgeo.2007.02.014.

Parrish, R. R. (1990), U-Pb dating of monazite and its application to geological problems, *Can. J. Earth Sci., 27*, 1431–1450, doi:10.1139/e90-152.

Passchier, C. W., and R. A. J. Trouw (2005), *Microtectonics,* Springer Verlag, Berlin.

Patel, R. C., and A. Carter (2009), Exhumation history of the Higher Himalayan Crystalline along Dhauliganga- Goriganga river valleys, NW India: New constraints from fission track analysis, *Tectonics, 28*, TC3004, doi:10.1029/2008TC002373.

Patel, R. C., S. Singh, A. Asokan. R. M. Manickavasagam, and A. K. Jain (1993), Extensional tectonics in the Himalayan orogen, Zanskar, NW India, in *Himalayan Tectonics*, edited by P. J. Treloar and M. P. Searle, *Geol. Soc. Spec. Publ., 74*, 445–459, doi:10.1144/GSL.SP.1993.074.01.30.

Paterson, S. R., R. H. Vernon, and O. T. Tobisch (1989), A review of criteria for the identification of magmatic and tectonic foliations in granitoids, *J. Struct. Geol., 11*, 349–363, doi:10.1016/0191-8141(89)90074-6.

Paterson, S. R., T. K. Fowler, K. L. Schmidt, A. S. Yoshinobu, E. S. Yuan, and R. B. Miller (1998), Interpreting magmatic fabric patterns in plutons, *Lithos*, *44*, 53–82, doi:10.1016/S0024-4937(98)00022-X.

Pattison, D. R. M. (1992), Stability of andalusite and sillimanite and the Al_2SiO_5 triple point: constraints from the Ballachulish aureole, Scotland, *J. Geol., 100*, 423–446.

Piazolo, S., and C. S. Passchier (2002), Controls on lineation development in low to medium grade shear zones: a study from the Cap de Creus peninsula, NE Spain, *J. Struct. Geol., 24,* 25–44, doi:10.1016/S0191-8141(01)00045-1.

Powell, R., and T. J. B. Holland (1994), Optimal geothermometry and geobarometry, *Am. Mineral., 79*, 120–133.

Powell, R., and T. J. B. Holland (2008), On thermobarometry, *J. Metamorph. Geol., 26*, 155–179, doi:10.1111/j.1525-1314.2007.00756.x.

Prince, C. P., N. Harris, and D. Vance (2001), Fluid enhanced melting during prograde metamorphism. *J. Geol. Soc. London, 158*, 233–241, doi: 10.1144/jgs.158.2.233.

Pyle, J. M., and F. S. Spear (1999), Yttrium zoning in garnet: coupling of major and accessory phases during metamorphic reactions, *Geol. Mat. Res., 1*, 1–49.

Pyle, J. M., and F. S. Spear (2003), Four generations of accessory-phase growth in low-pressure migmatites from SW New Hampshire, *Am. Mineral., 88*, 338–351, doi:10.2138/am-2003-2-311.

Robinson, D. M., P. G. DeCelles, and P. Copeland (2006), Tectonic evolution of the Himalayan thrust belt in western Nepal: Implications for channel flow models, *Geol. Soc. Am. Bull., 118*, 865–885, doi:10.1130/B25911.1.

Roper, P. J. (1972), Structural significance of ''button'' or ''fish scale'' texture in the phyllonitic schist of the Brevard zone, *Geol. Soc. Am. Bull., 83*, 853–860, doi:10.1130/0016-7606(1972)83[853:SSOBOF].

Rosenberg, C. L., and M. R. Handy (2001), Mechanisms and orientation of melt segregation paths during pure shearing of a partially molten rock analog (norcamphor–benzamide), *J. Struct. Geol., 23*, 1917–1932, doi:10.1016/S0191-8141(01)00037-2.

Rubatto, D., S. Chakraborty, and S. Dasgupta (2013), Timescale of crustal melting in the Higher Himalayan Crystallines (Sikkim, Eastern Himalaya) inferred from trace element-constrained monazite and zircon chronology, *Contrib. Mineral. Petrol., 165*, 349–372, doi:10.1007/s00410-012-0812-y.

Rubatto, D., I. S. Williams, and I. S. Buick (2001), Zircon and monazite response to prograde metamorphism in the Reynolds Range, Central Australia, *Contrib. Mineral. Petrol., 140*, 458–468, doi:10.1007/PL00007673.

Sachan, H. K., M. J. Kohn, A. Saxena, and S. L. Corrie (2010), The Malari leucogranite, Garhwal Himalaya, northern India: chemistry, age, and tectonic implications, *Geol. Soc. Am. Bull., 122*, 1865–1876, doi:10.1130/B30153.1.

Saxena, A., H. K. Sachan, P. K. Mukherjee, and D. K. Mukhopadhya (2012), Fluid–rock interaction across the South Tibetan Detachment, Garhwal Himalaya (India): Mineralogical and geochemical evidences, *J. Earth Syst. Sci., 121*, 29–44, doi:10.1007/s12040-012-0145-2.

Schultz, M. H., K. V. Hodges, T. A. Ehlers, M. van Soest, and J. -A. Wartho (2017), Thermochronologic constraints on the slip history of the South Tibetan detachment system in the Everest region, southern Tibet, *Earth Planet. Sci. Lett., 459,* 105–117, doi:10.1016/j.epsl.2016.11.022.

Sciunnach, D., and E. Garzanti (2012), Subsidence history of the Tethys Himalaya, *Earth Sci. Rev., 111*, 179–198, doi:10.1016/j.earscirev.2011.11.007.

Searle M. P., and L. Godin (2003), The South Tibetan detachment and the Manaslu Leucogranite; a structural reinterpretation and restoration of the Annapurna–Manaslu Himalaya, Nepal, *J. Geol., 111*, 505–523, doi:10.1086/376763.

Searle, M. P. (1999), Extensional and compressional faults in the Everest-Lhotse massif, Khumbu Himalaya, Nepal, *J. Geol. Soc., 156*, 227–240, doi:10.1144/gsjgs.156.2.0227.

Searle, M. P. (2010), Low-angle normal faults in the compressional Himalayan orogen; evidence from the Annapurna–Dhaulagiri Himalaya, Nepal, *Geosphere, 6,* 296–315, doi:10.1130/GES00549.1.

Sen, K., R. Chaudhurya, and J. Pfänder (2015), $^{40}Ar–^{39}Ar$ age constraint on deformation and brittle–ductile transition of the Main Central Thrust and the South Tibetan Detachment zone from Dhauliganga valley, Garhwal Himalaya, India, *J. Geodyn., 88*, 1–13, doi:10.1016/j.jog.2015.04.004.

Seydoux-Guillaume, A. M., J. L. Paquette, M. Wiedenbeck, J. M. Montel, and W. Heinrich (2002a), Experimental resetting of the U–Th–Pb system in monazite, *Chem. Geol., 191*, 165–181, doi:10.1016/S0009-2541(02)00155-9.

Seydoux-Guillaume, A. M., R. Wirth, L. Nasdala, M. Gottschalk, J. M. Montel, and W. Heinrich (2002b), XRD, TEM and Raman study of experimental annealing of natural monazite, *Phys. Chem. Min., 29*, 240–253, doi:10.1007/s00269-001-0232-4.

Shreshtha, M., Jain, A.K., and S. Singh (2015), Shear sense analysis of the Higher Himalayan Crystalline (HHC) belt, and tectonics of the South Tibetan Detachment System (STDS), Alaknanda – Dhauli Ganga Valley, Uttarakhand Himalaya, *Current Sci., 108 (6)*, 1107–1118.

Simpson, C., and D. G. De Paor (1993), Strain and kinematic analysis in general shear zones. *J. Struct. Geol., 15*, 1–20, doi:10.1016/0191-8141(93)90075-L.

Soucy-La Roche, R., L. Godin, J. M. Cottle, and D. A. Kellett (2016), Direct shear fabric dating constrains early Oligocene onset of the South Tibetan detachment in the western Nepal Himalaya, *Geology, 44*, 403–406, doi:10.1130/G37754.1.

Spear, F. S. (1991), On the interpretation of peak metamorphic temperatures in the of garnet diffusion during cooling, *J. Metamorph. Geol., 9,* 379–388, doi:10.1111/j.1525-1314.1991.tb00533.x.

Spear, F. S. (1993), *Metamorphic Phase Equilibria and Pressure-Temperature-Time Paths*, 779 pp., Mineral. Soc., of Am., Washington, D. C.

Spear, F. S. (2010), Monazite–allanite phase relations in metapelites, *Chem. Geol., 279,* 55–62, doi:10.1016/j.chemgeo.2010.10.004.

Spear, F. S., and F. P. Florence (1992), Thermobarometry in granulites: pitfalls and new approaches, *Precambrian Res., 55*, 209–241, doi:10.1016/0301-9268(92)90025-J.

Spear, F. S., and J. M. Pyle (2002), Apatite, monazite, and xenotime in metamorphic rocks, *Rev. Mineral. Geochem.*, *48*, 293–335, doi:10.2138/rmg.2002.48.7.

Spear, F. S., and J. M. Pyle (2010), Theoretical modelling of monazite growth in a low-Ca metapelite, *Chem. Geol., 273*, 111–119, doi:10.1016/j.chemgeo.2010.02.016.

Spear, F. S., M. J. Kohn, and J. T. Cheney (1999), P-T paths from anatectic pelites, *Contrib. Mineral. Petrol., 134*, 17–32, doi:10.1007/s004100050466.

Spencer, C. J., R. A. Harris, and M. J. Dorais (2012a), Depositional provenance of the Himalayan metamorphic core of Garhwal region, India: Constrained by U–Pb and Hf isotopes in zircons, *Gondwana Res., 22*, 26–35, doi:10.1016/j.gr.2011.10.004.

Spencer, C. J., R. A. Harris, and M. J. Dorais (2012b), The metamorphism and exhumation of the Himalayan metamorphic core, eastern Garhwal region, India, *Tectonics, 31*, TC1007, doi:10.1029/2010TC002853.

Stipp, M., H. Stunitz, R. Heilbronner, and S. M. Schmid (2002a), The eastern Tonale fault zone: A 'natural laboratory' for crystal plastic deformation over a temperature range from 250 to 700 °C, *J. Struct. Geol., 24*, 1861–1884, doi:10.1016/S0191-8141(02)00035-4.

Stipp, M., H. Stunitz, R. Heilbronner, and S. M. Schmid (2002b), Dynamic recrystallization of quartz: correlation between natural and experimental conditions, in *Deformation Mechanisms, Rheology and Tectonics: Current Status and Future Perspectives,* edited by S. De Meer et al., *Geol. Soc. Spec. Publ.*, *200*, 171–190.

Tera, F., and G. J. Wasserburg (1972), U-Th-Pb systematics in three Apollo 14 basalts and the problem of initial Pb in lunar rocks, *Earth Planet. Sc. Lett., 14*, 281–304, doi:10.1016/0012-821X(72)90128-8.

Thakur, S. S., S. C. Patel, and A. K. Singh (2015), A P-T pseudosection modelling approach to understand metamorphic evolution of the Main Central Thrust Zone in the Alaknanda valley, NW Himalaya, *Contrib. Mineral. Petrol., 170*, 1–26, doi:10.1007/s00410-015-1159-y.

Tomkins, H. S., and D. R. M. Pattison (2007), Accessory phase petrogenesis in relation to major phase assemblages in pelites from the Nelson contact aureole, southern British Columbia, *J. Metamorph. Geol., 25*, 401–421, doi:10.1111/j.1525-1314.2007.00702.x.

Tracy, R. J., P. Robinson, and A. B. Thompson (1976), Garnet composition and zoning in the determination of temperature and pressure of metamorphism, central Massachusetts, *Am. Mineral., 61*, 762-775.

Tullis, J., and R. A. Yund (1977), Experimental deformation of dry Westerly granite, *J. Geophys. Res., 82*, 5705–5718, doi:10.1029/JB082i036p05705.

Valdiya, K. S., S. K. Paul, S. S. Tarachandra-Bhakuni, and R.C. Upadhyay (1999), Tectonic and Iithological characterization of Himadri (Great Himalaya) between Kali and Yamuna rivers, Central Himalaya, *Himalayan Geol., 10*, 1–17.

van Achterbergh, E., C. G. Ryan, S. E. Jackson, and W. Griffin (2001), Data reduction software for LA-ICP-MS, in *Laser Ablation-ICPMS in the Earth Science: Principles and Applications*, edited by P. Sylvester, *Mineral. Ass. Can., 29*, 239-243.

Vannay, J. C., and K. V. Hodges (1996), Tectonometamorphic evolution of the Himalayan metamorphic core between Annapurna and Dhaulagiri, central Nepal, *J. Metamorph. Geol., 14*, 635–656, doi:10.1046/j.1525-1314.1996.00426.x.

Vernon, R. H. (2011), Microstructures of melt-bearing regional metamorphic rocks, *Geol. Soc. Am. Mem., 207*, 1–11, doi:10.1130/2011.1207(01).

Viskupic, K., K. V. Hodges, and S. A. Bowring (2005), Timescales of melt generation and the thermal evolution of the Himalayan metamorphic core, Everest region, eastern Nepal, *Contrib. Mineral. Petrol., 149*, 1–21, doi:10.1007/s00410-004-0628-5.

Visonà, D., and B. Lombardo (2002), Two-mica and tourmaline leucogranites from Everest–Makalu region (Nepal–Tibet). Himalayan leucogranites genesis by isobathic heating?, *Lithos, 62*, 125–150, doi:10.1016/S0024-4937(02)00112-3.

Visonà, D., R. Carosi, C. Montomoli, M. Peruzzo, and L. Tiepolo (2012), Miocene andalusite leucogranite in central-east Himalaya (Everest–Masang Kang area): low-pressure melting during heating, *Lithos, 144*, 194–208, doi:10.1016/j.lithos.2012.04.012.

Wang, J. -M., J. -J. Zhang, K. Liu, B. Zhang, X. -X. Wang, S. M. Rai, and M., Scheltens (2016), Spatial and temporal evolution of tectonometamorphic discontinuities in the central Himalaya: Constraints from P–T paths and geochronology, *Tectonophysics, 679*, 41–60, doi:10.1016/j.tecto.2016.04.035.

Weinberg, R. F. (2016), Himalayan leucogranites and migmatites: nature, timing and duration of anataxis, *J. Metamorph. Geol., 34,* 821–843, doi:10.1111/jmg.12204.

Wernicke, B. (1981), Low angle normal faults in the Basin and Range Province: Nappe tectonics in an extending orogene, *Nature, 291*, 645–648, doi:10.1038/291645a0.

Wernicke, B. (2009), The detachment era (1977–1982) and its role in revolutionizing continental tectonics, in *Extending a Continent: Architecture, Rheology and Heat*

Budget, edited by U. Ring and B. Wernicke, *Geol. Soc. Spec. Publ.*, *321*, 1–8, doi:10.1144/SP321.1.

Williams, M. L., and M. J. Jercinovic (2002), Microprobe monazite geochronology: putting absolute time into microstructural analysis, *J. Struct. Geol., 24*, 1013–1028, doi:10.1016/S0191-8141(01)00088-8.

Williams, M. L., and M. J. Jercinovic (2012), Tectonic interpretation of metamorphic tectonites: integrating compositional mapping, microstructural analysis and in situ monazite dating, *J. Metamorph. Geol.*, *30*, 739–752, doi:10.1111/j.1525-1314.2012.00995.x.

Williams, M. L., M. J. Jercinovic, D. E. Harlov, B. Budzýn, and C. J. Hetherington (2011), Resetting monazite ages during fluid-related alteration, *Chem. Geol., 283,* 218–225, doi: 10.1016/j.chemgeo.2011.01.019.

Williams, M. L., M. J. Jercinovic, and C. J. Hetherington (2007), Microprobe Monazite Geochronology: Understanding Geologic Processes by Integrating Composition and Chronology, *Annu. Rev. Earth Pl. Sci., 35*, 137–175, doi:10.1146/annurev.earth.35.031306.140228.

Wing, B. A., J. M. Ferry, and T. M. Harrison (2003), Prograde destruction and formation of monazite and allanite during contact and regional metamorphism of pelites: petrology and geochronology, *Contrib. Mineral. Petrol., 145*, 228–250, doi:10.1007/s00410-003-0446-1.

Xypolias, P. (2010), Vorticity analysis in shear zones: a review of methods and applications, *J. Struct. Geol.*, *32*, 2072–2092, doi:10.1016/j.jsg.2010.08.009.

Yakymchuk, C., and M. Brown (2014), Behaviour of zircon and monazite during crustal melting, *J. Geol. Soc. London, 171*, 465–479, doi:10.1144/jgs2013-115.

Waizenhöfer, F., and H. -J. Massonne (2017), Monazite in a Variscan mylonitic paragneiss from the Münchberg Metamorphic Complex (NE Bavaria) records Cadomian protolith ages, *J. Metamorph. Geol.*, *35,* 453–469, doi:10.1111/jmg.12240.

Table 1. Selected mineral compositions of sample GW13-62. Structural formulae were calculated as follows: garnet = 24 O; feldspar = 8 O; biotite and white mica = 11 O; b.d. = below the detection limit.

mineral:	Garnet			Biotite		White mica	Plagioclase		K-feldspar	
position:	core	middle	rim	matrix	near Grt	late	matrix	matrix	matrix	matrix
wt.%										
SiO_2	35.86	37.40	36.80	34.43	34.30	44.49	60.38	59.40	63.48	63.34
TiO_2	0.00	0.00	0.02	4.73	2.88	0.05	b.d.	0.01	b.d.	0.01
Al_2O_3	21.07	21.46	21.40	18.57	19.11	33.75	25.03	25.12	17.98	18.12
Cr_2O_3	0.02	0.01	0.00	–	–	–	–	–	–	–
FeO_{tot}	33.40	34.08	34.63	19.84	19.69	2.57	0.16	0.20	0.04	0.05
MnO	2.56	2.31	3.23	0.16	0.11	0.04	0.01	0.01	0.01	b.d.
MgO	4.38	4.21	3.32	7.76	8.50	0.94	b.d.	b.d.	b.d.	b.d.
CaO	2.52	2.06	1.56	0.03	0.00	0.03	6.58	7.03	0.04	0.06
BaO	–	–	–	0.31	0.23	0.10	0.01	0.02	0.39	0.23
Na_2O	0.03	0.00	0.00	0.11	0.16	0.16	7.95	7.61	0.46	0.91
K_2O	–	–	–	9.93	9.84	10.88	0.20	0.15	16.59	16.05
Sum	99.84	100.53	100.96	95.87	94.82	93.02	100.41	99.56	98.99	98.77
Element										
Si	5.581	5.823	5.792	2.636	2.648	3.063	2.682	2.662	2.987	2.980
Al^{IV}	0.419	0.177	0.208	1.364	1.352	0.937	1.310	1.327	0.997	1.005
Ti	0.000	0.000	0.002	0.270	0.167	0.003	0.000	0.000	0.000	0.000
Al^{VI}	3.446	3.760	3.762	0.311	0.387	1.801	–	–	–	–
Cr	0.003	0.002	0.000	–	–	–	–	–	–	–
Fe^{3+}	0.132	0.062	0.030	0.000	0.000	0.026	0.006	0.008	0.002	0.002
Fe^{2+}	4,215	4.375	4.528	1.270	1.271	0.122	–	–	–	–
Mn	0.338	0.304	0.431	0.010	0.007	0.002	0.000	0.000	0.000	0.000
Mg	1.017	0.978	0.778	0.886	0.979	0.096	0.000	0.000	0.000	0.000
Ca	0.338	0.343	0.263	0.003	0.000	0.003	0.313	0.337	0.002	0.003
Ba	–	–	–	0.009	0.007	0.003	0.000	0.000	0.007	0.004
Na	0.009	0.000	0.000	0.016	0.024	0.022	0.685	0.661	0.042	0.083
K	–	–	–	0.970	0.969	0.956	0.012	0.009	0.996	0.963
Sum	15.498	15.824	15.794	7.745	7.811	7.033	5.008	5.006	5.033	5.040

Table 2. Selected compositions of monazite from sample GW13-62 normalized to 4 O. P domain = biotite rich-domain; Q Domain = quartzo-feldspathic domain; b.d. = below the detection limit.

	Mnz1 P domain		Mnz3 Q domain		Mnz4 Q domain		Mnz5 Q domain		Mnz6 P domain	
	core	rim	core	rim	core	rim	core	rim	core	rim
wt.%										
SiO_2	0.77	0.15	0.92	0.43	0.60	0.25	0.41	0.35	0.42	0.29
P_2O_5	28.66	29.90	28.51	29.64	29.19	29.87	29.60	30.02	29.27	29.91
CaO	1.48	1.00	1.41	1.12	1.18	1.14	1.11	1.06	1.06	1.15
Y_2O_3	0.26	2.91	0.38	1.80	0.14	2.98	0.32	2.05	0.15	1.78
La_2O_3	13.71	12.19	13.05	12.95	13.96	12.41	13.96	12.72	13.81	12.62
Ce_2O_3	28.32	27.07	27.79	28.26	29.65	27.06	29.64	27.74	30.19	28.56
Pr_2O_3	3.17	3.33	2.83	3.19	3.31	3.09	3.64	2.90	3.16	3.31
Nd_2O_3	10.59	11.71	10.71	11.60	11.53	11.28	11.47	11.52	11.54	10.93
Sm_2O_3	1.74	2.60	2.08	2.01	1.97	2.48	2.03	2.47	1.87	2.19
Eu_2O_3	b.d.	b.d.	b.d.	b.d.	b.d.	b.d.	b.d.	b.d.	b.d.	b.d.
Gd_2O_3	0.95	2.71	1.42	2.00	1.01	2.52	1.63	2.50	1.08	2.08
ThO_2	7.94	4.27	9.54	6.25	6.64	5.61	5.98	4.54	5.85	5.54
UO_2	1.06	0.48	0.68	0.00	0.89	0.20	0.22	0.63	0.68	0.56
Sum	98.64	98.33	99.32	99.26	100.06	98.88	100.01	98.50	99.08	98.92
Element										
Si	0.031	0.006	0.037	0.017	0.024	0.010	0.016	0.014	0.017	0.011
P	0.974	0.999	0.968	0.989	0.979	0.995	0.988	1.000	0.988	0.998
Ca	0.064	0.042	0.061	0.048	0.050	0.048	0.047	0.045	0.045	0.048
Y	0.005	0.061	0.008	0.038	0.003	0.062	0.007	0.043	0.003	0.037
La	0.203	0.177	0.193	0.188	0.204	0.180	0.203	0.185	0.203	0.183
Ce	0.416	0.391	0.408	0.408	0.430	0.390	0.428	0.400	0.441	0.412
Pr	0.046	0.048	0.041	0.046	0.048	0.044	0.052	0.042	0.046	0.048
Nd	0.152	0.165	0.153	0.163	0.163	0.159	0.162	0.162	0.164	0.154
Sm	0.024	0.035	0.029	0.027	0.027	0.034	0.028	0.033	0.026	0.030
Eu	0.000	0.000	0.000	0.000	0.000	0.000	0.000	0.000	0.000	0.000
Gd	0.013	0.035	0.019	0.026	0.013	0.033	0.021	0.033	0.014	0.027
Th	0.065	0.034	0.078	0.050	0.053	0.045	0.048	0.036	0.047	0.044
U	0.009	0.004	0.006	0.000	0.008	0.002	0.002	0.006	0.006	0.005
Sum	2.003	2.000	2.001	2.001	2.002	2.001	2.001	1.997	2.000	1.998

Table 3. LA-ICP-MS U-(Th)-Pb *in situ* geochronological results. P domain = biotite-rich domain, Q domain = quartzo-feldspathic domain, % D. = percentage of discordance calculated as [1- (^{208}Pb/^{232}Th / ^{206}Pb/^{238}U)] × 100. The amount of Y_2O_3 wt%, determined by EMPA, close to the ablation pit is indicated. Mnz-type-A and Mnz-type-B are texturally and chemically defined as reported in the main text.

Mnz grain	Grain Position	Spot location	Y_2O_3 wt%	Mnz type	Isotopic ratio						Ages (Ma)						
					^{207}Pb/^{235}U	1σ abs	^{206}Pb/^{238}U	1σ abs	^{208}Pb/^{232}Th	1σ abs	^{207}Pb/^{235}U	1σ abs	^{206}Pb/^{238}U	1σ abs	^{208}Pb/^{232}Th	1σ abs	% D.
1	P domain	core	0.25	A	0.03194	0.00085	0.00361	0.00005	0.00096	0.00001	32	0.9	23	0.3	19	0.3	17
1	P domain	core	0.51	A	0.03262	0.00070	0.00384	0.00005	0.00104	0.00001	33	0.7	25	0.3	21	0.3	16
1	P domain	core	0.26	A	0.03581	0.00094	0.00389	0.00005	0.00099	0.00001	36	0.9	25	0.3	20	0.3	20
2	P domain	rim	2.91	B	0.03336	0.00089	0.00339	0.00005	0.00092	0.00001	33	0.9	22	0.3	19	0.3	14
2	P domain	rim	2.00	B	0.03922	0.00105	0.00353	0.00005	0.00095	0.00001	39	1.0	23	0.3	19	0.3	17
2	P domain	core	0.13	A	0.03579	0.00092	0.00389	0.00005	0.00106	0.00002	36	0.9	25	0.3	21	0.4	16
2	P domain	core	0.45	A	0.03661	0.00079	0.00394	0.00005	0.00104	0.00001	37	0.8	25	0.3	21	0.3	16
6	P domain	core	0.15	A	0.04393	0.00102	0.00377	0.00005	0.00103	0.00001	44	1.0	24	0.3	21	0.3	13
6	P domain	core	1.57	B	0.03409	0.00079	0.00380	0.00005	0.00103	0.00001	34	0.8	24	0.3	21	0.3	13
3	Q domain	core	0.14	A	0.04791	0.00128	0.00411	0.00006	0.00116	0.00002	48	1.3	26	0.4	23	0.5	12
7	P domain	core	0.42	A	0.03409	0.00086	0.00346	0.00005	0.00088	0.00001	34	0.9	22	0.3	18	0.3	18
7	P domain	rim	1.78	B	0.03982	0.00125	0.00327	0.00005	0.00078	0.00001	40	1.2	21	0.3	16	0.2	24
7	P domain	core	0.34	A	0.03655	0.00087	0.00371	0.00005	0.00103	0.00001	37	0.9	24	0.3	21	0.3	13

| 5	Q domain	core	0.32	A	0.04561	0.00155	0.00405	0.00006	0.00103	0.00002	45	1.5	26	0.4	21	0.4	19
5	Q domain	rim	2.05	B	0.04062	0.00096	0.00386	0.00005	0.00098	0.00001	40	1.0	25	0.3	20	0.3	20
4	P domain	core	0.14	A	0.03366	0.00071	0.00389	0.00005	0.00112	0.00002	34	0.7	25	0.3	23	0.5	8
4	P domain	rim	2.98	B	0.03322	0.00070	0.00380	0.00005	0.00106	0.00002	33	0.7	24	0.3	21	0.4	13
4	P domain	rim	1.44	B	0.03196	0.00070	0.00369	0.00005	0.00104	0.00001	32	0.7	24	0.3	21	0.3	13
4	P domain	core	0.27	A	0.03307	0.00073	0.00377	0.00005	0.00106	0.00002	33	0.7	24	0.3	21	0.4	13
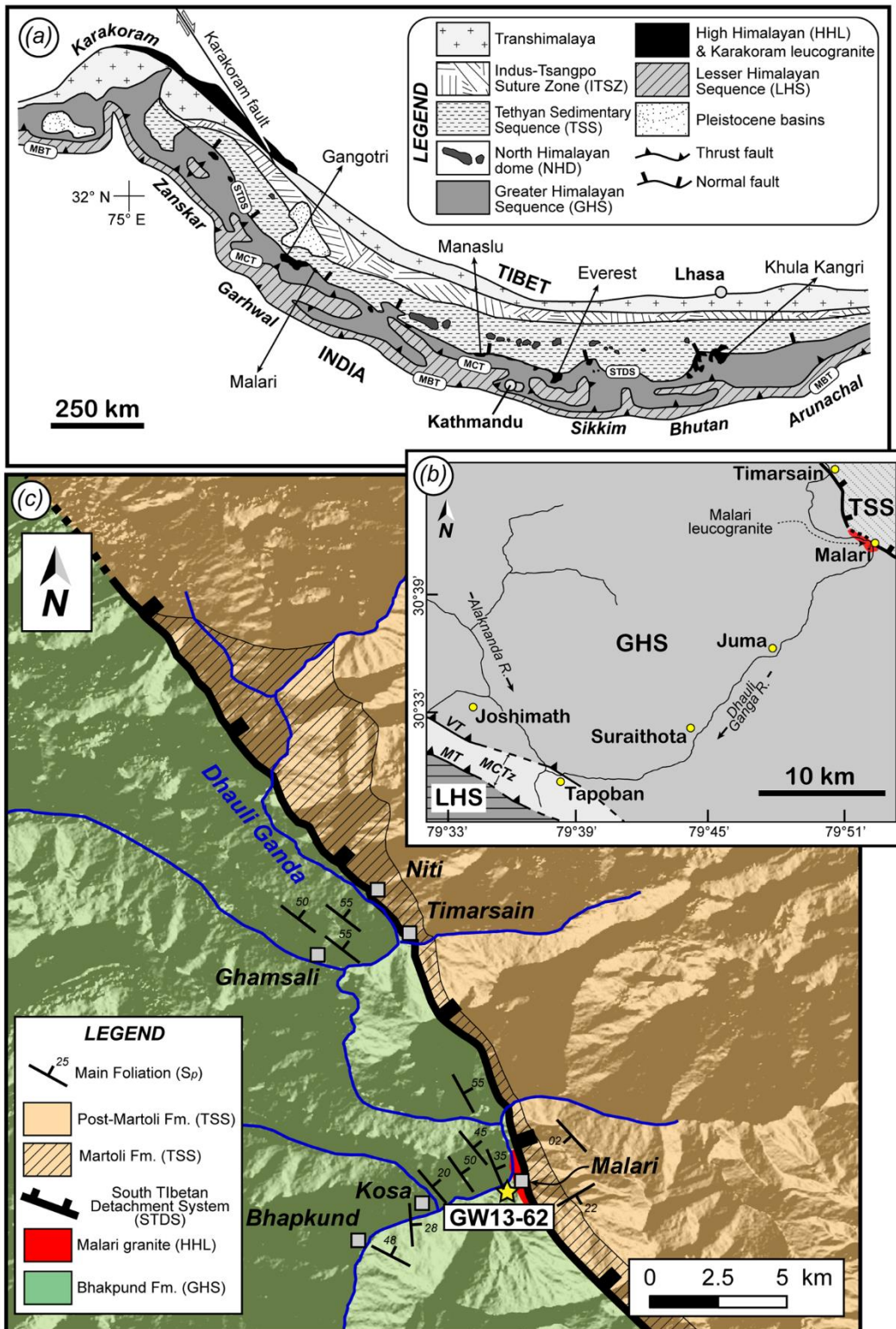
Figure 1. (a) Geological map of the Himalaya, after *Weinberg* [2016]. (b) Geological sketch

of the Alaknanda-Dhauli Ganga valleys (Garhwal Himalaya, NW India) after *Spencer et al.*

[2012a, b] and *Jain et al.* [2014]. (c) Detailed geological map in the area around the village of

Malari. Location of sample GW13-62, selected for detailed investigations, is indicated by a yellow star.
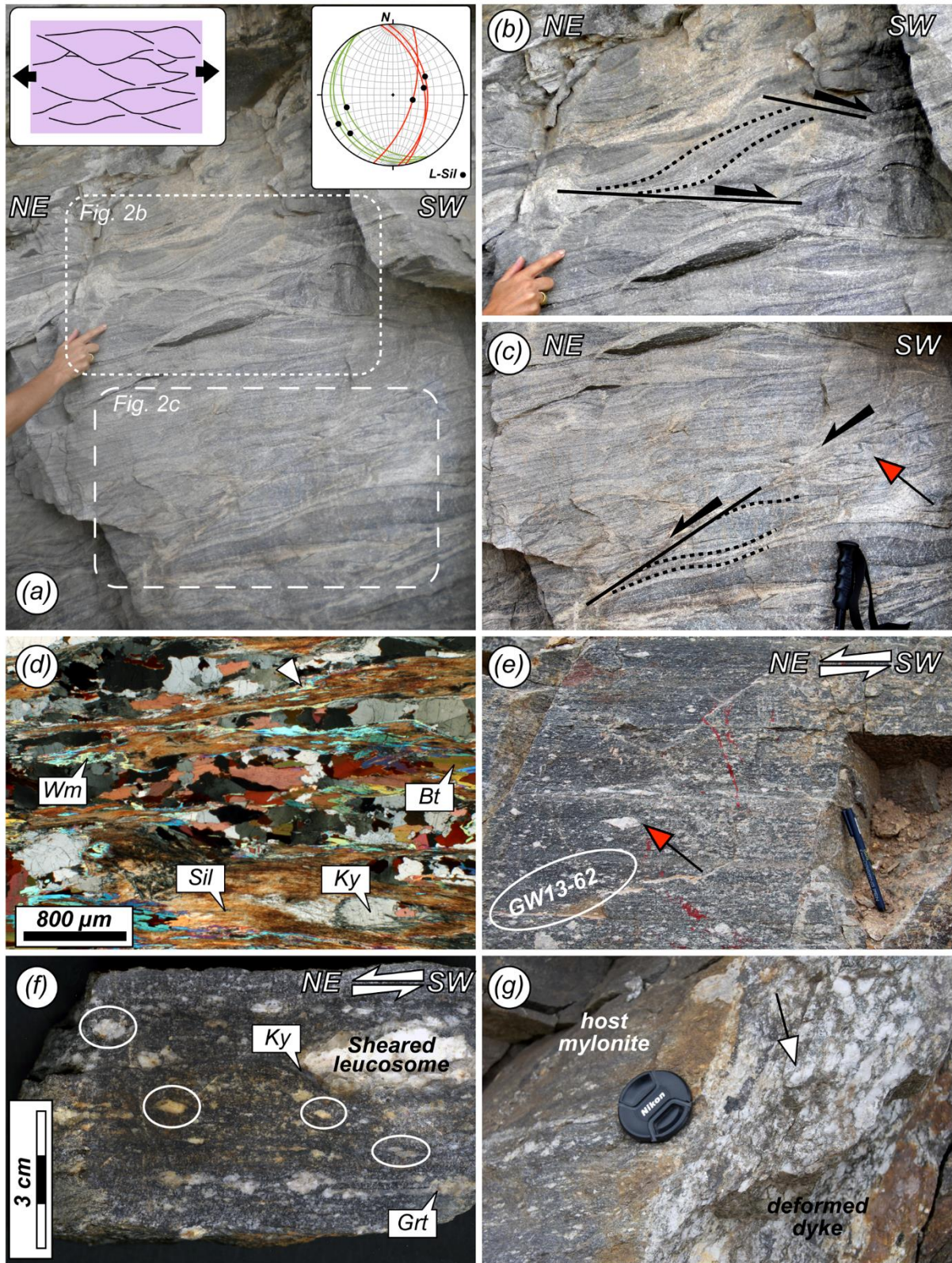
Figure 2. Photographs of sheared migmatite in the upper GHS. (a) Conjugate sillimanite-

bearing shear bands (arrows) in migmatite. In the upper-left insert a sketch of conjugate shear

zones is shown. Upper-right insert: stereoplot (Wulff net, lower hemisphere) of the conjugate

sillimanite-bearing shear bands and the mineral lineation (L-Sil). (b) Deflection of the main foliation along shear bands, containing sillimanite, pointing to a top-down-to-the-SW sense of shear (arrows). (c) Close to a top-down-to-the-NE sillimanite-bearing shear band, as supported by the offset of pre-existing markers and by drag folds (red arrow). (d) Syn-kinematic sillimanite (after kyanite) and minor late white mica (arrow) growing on shear bands. (e) HT-mylonite, showing normal top-to-the-NE shearing (see red arrow), being a deformed migmatitic paragneiss. White ellipse shows the location of sample GW13-62. (f) Polished hand sample of HT-mylonite, where feldspar porphyroclasts (white ellipses) support a normal top-to-the-NE sense of shear. Note the stretched leucosome. (g) Deformed pegmatitic dyke oriented at high-angle with respect to the mylonitic foliation. Mineral abbreviations: Bt = biotite, Grt = garnet, Ky = kyanite, Sil = sillimanite, Wm = white mica.
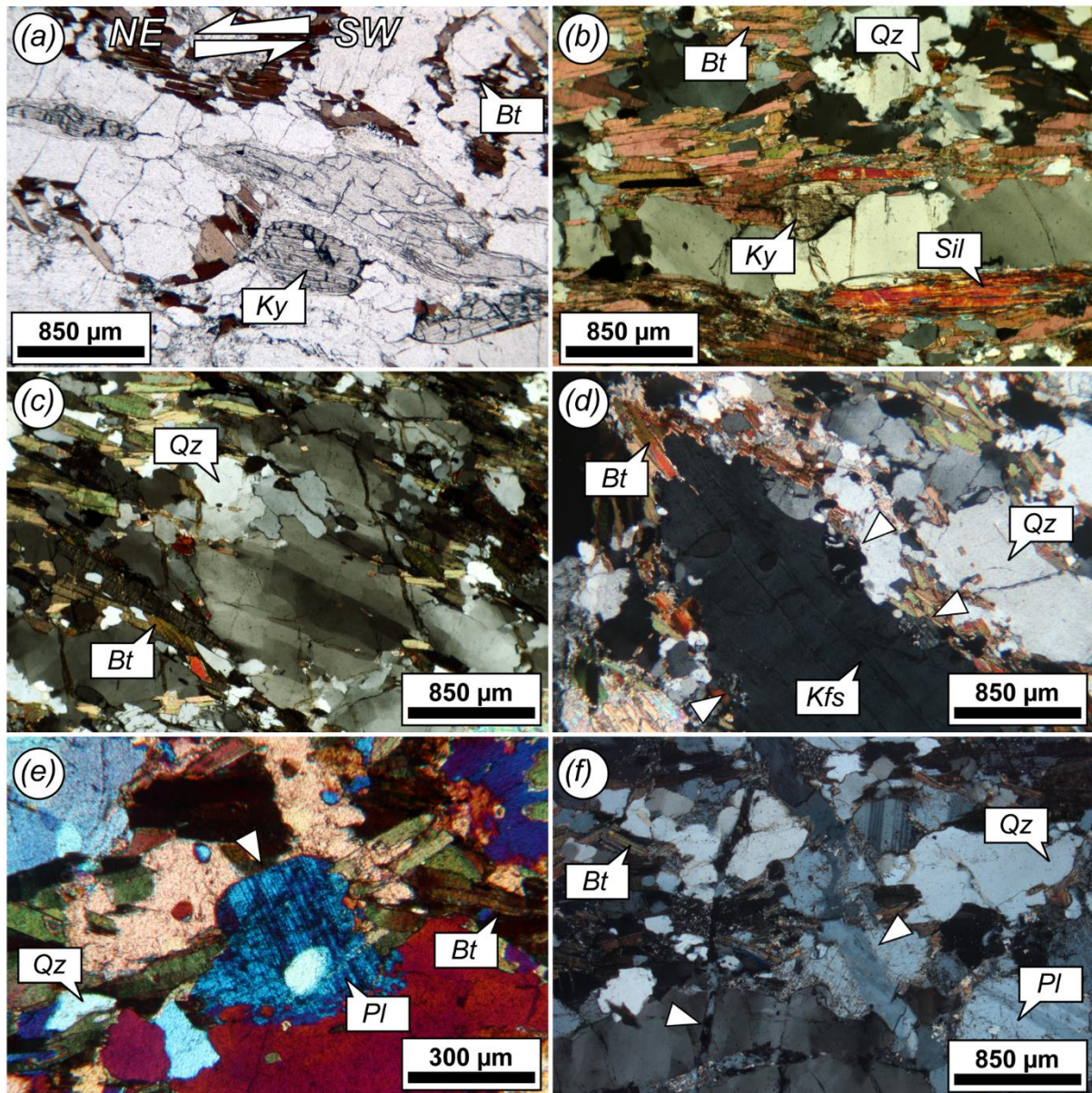
Figure 3. Photomicrographs of HT-mylonite from the upper GHS. (a) Kyanite porphyroclast pointing to a normal top-to-the-NE sense of shear. (b) Mylonitic foliation defined by sillimanite (after kyanite) and reddish-brownish biotite (sample GW13-62). (c) Chessboard extinction pattern in quartz. (d) K-feldspar porphyroclast with myrmekite (arrows). (e) Euhedral faces of plagioclase (melt-precipitated) in low-strain domains. (f) Rare late transgranular fractures (arrows) filled by quartz and feldspar. Mineral abbreviations as in Figure 2 and Kfs = K-feldspar, Pl = plagioclase, Qz = quartz.
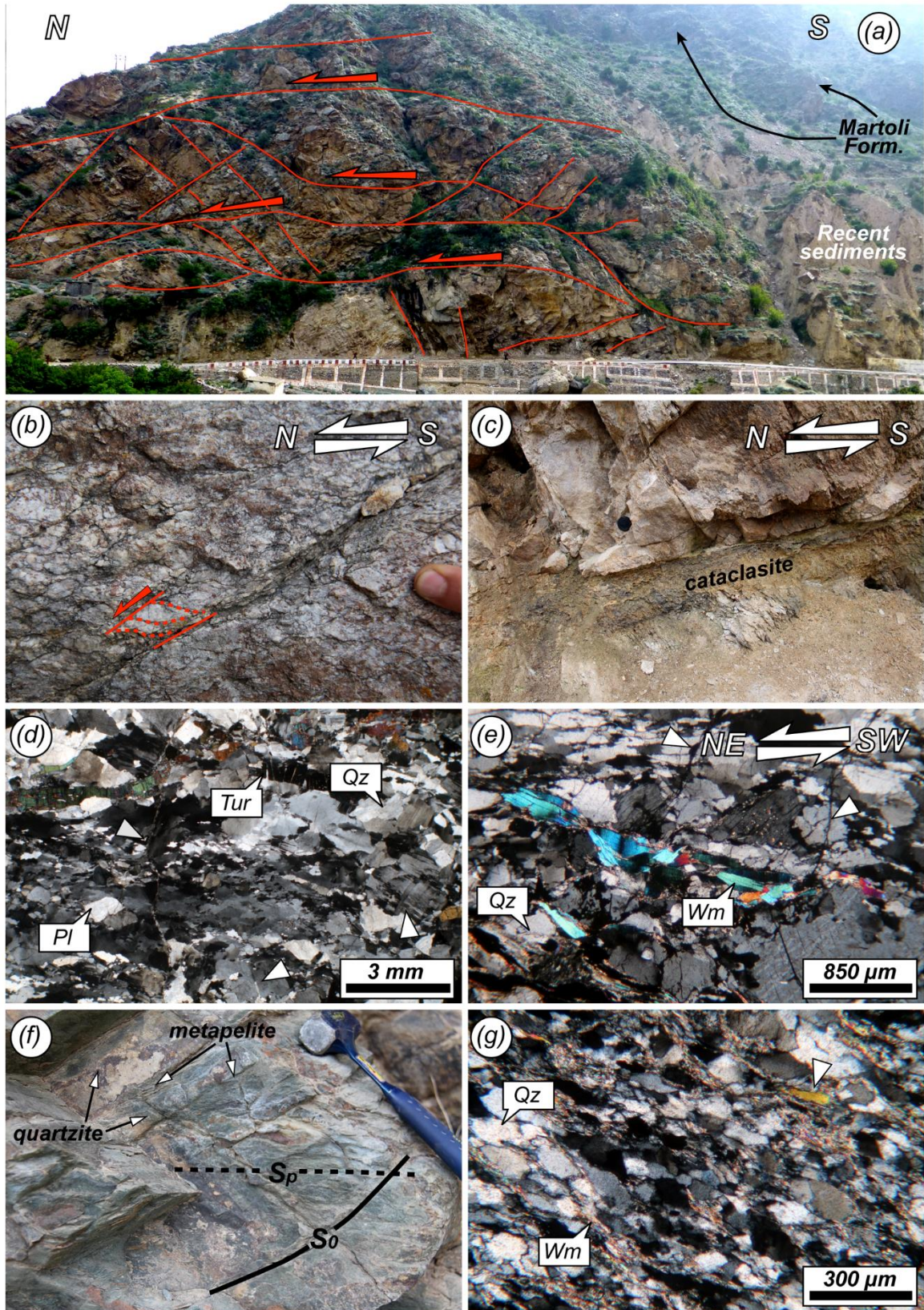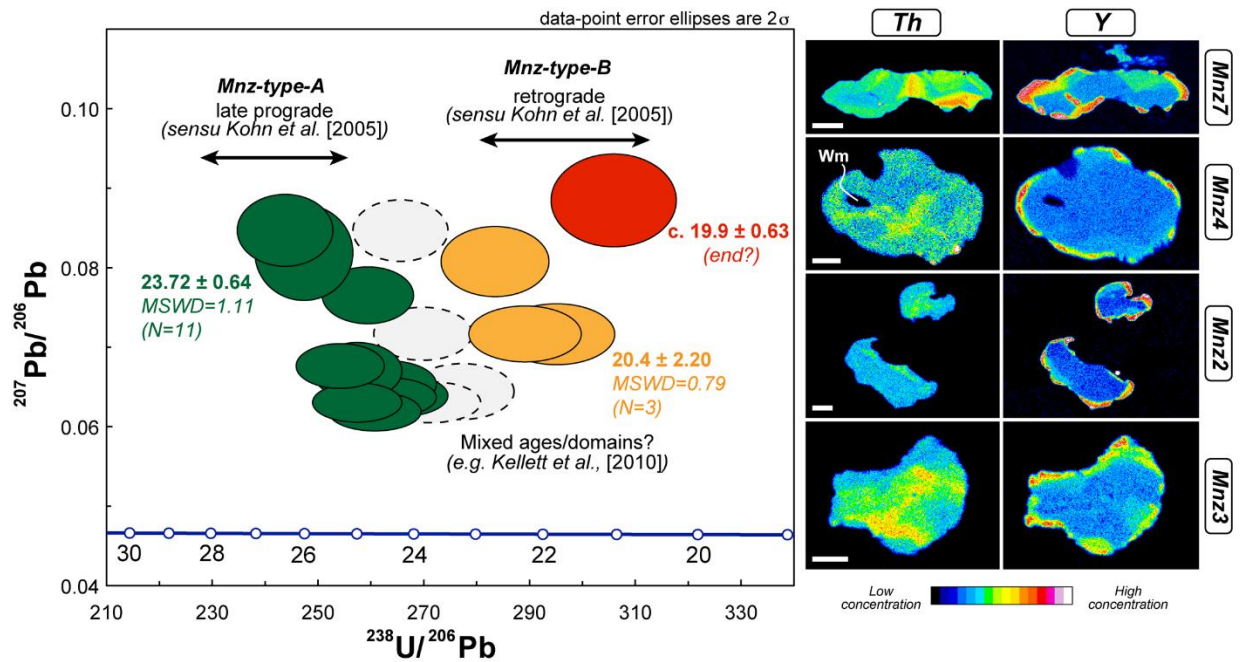
Figure 4. Outcrop and photomicrographs of the Malari granite and of the Martoli Formation

above (TSS – see Figure 1). (a) Panoramic view towards the village of Malari. Main brittle

faults, affecting the Malari granite and the leucogranitic dykes, are highlighted in red

(modified after *Jain et al*. [2014]). (b) Feldspar porphyroclasts and S-C-C' fabric in the

deformed Malari granite, pointing to a normal top-to-the-NE sense of shear. (c) Brittle

normal fault within the Malari granite. Note cataclastic core of the fault. (d) Overview

photomicrograph of Malari granite, showing dynamic recrystallization (SGR) of quartz,

deformation of feldspar (white arrow) and boudinage in tourmaline. (e) White-mica fish in

the Malari granite, pointing to a top-to-the-NE sense of shear. Note late transgranular

fractures (arrow). (f) Quartzite of the Martoli Formation showing the relationship between

bedding (S_0), defined by the intercalations of pelitic and quartz-rich layers (arrows), and main

foliation (S_p). (g) Low-grade quartzite of the Martoli Formation showing bulging

Recrystallization (BLG) of quartz and fine-grained white mica defining S_p. Note also detrital

white mica (arrow). Mineral abbreviation as reported in Figures 3 and Tur = tourmaline.

Figure 5. (a) P-T pseudosection for the HT-mylonite sample GW13-62. The bulk-rock composition plots in the wacke field according to the diagram by *Herron* [1988]. The inferred equilibrium assemblages are highlighted with different colors (M1 = blue, M2 = white). (b) Derived P-T path (red arrow) for sample GW13-62, based on isopleth intersections (see text) and THERMOCALC average P-T (AveP-T) calculations. Isopleths are defined as follows: XFe(Grt) = $Fe^{2+}/(Mg+Ca+Mn+Fe^{2+})$, XCa(Grt) = $Ca/(Mg+Ca+Mn+Fe^{2+})$, melt% = modal amount of melt, Grt% = modal amount of garnet. The dashed grey area represents the P-T uncertainty ellipse calculated according to *Powell and Holland* [1994]. Mineral abbreviations as in Figure 3 and Chl = chlorite, Crd = cordierite, Ilm = ilmenite, Opx = orthopyroxene, Pg = paragonite, Rt = rutile, L= silicate melt, V= aqueous fluid.

Figure 6. Tera-Wasserburg plot of isotopic ratios determined for selected monazite grains (sample GW13-62). On the right hand side a selection of representative X-ray compositional maps for Th and Y is shown (scale bar = 20 µm). Based on texture, chemistry and isotopic ratios two monazite populations were defined: Mnz-type-A forming core of grains with low-Y and high/medium Th+U contents, and Mnz-type-B forming high-Y rims. See text, Table 2 and Table 3 for more details.
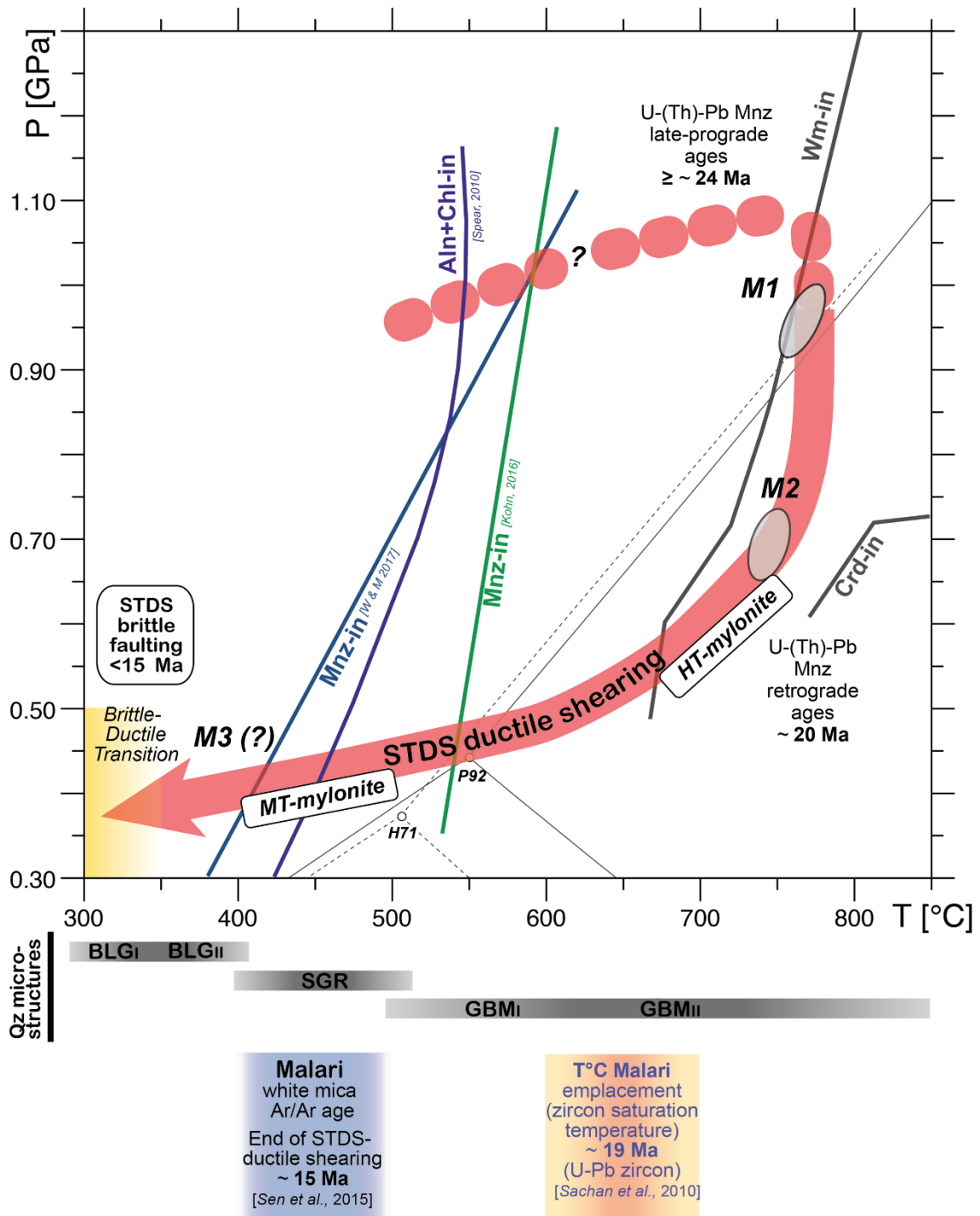
Figure 7. P-T-D-t path for the STDS-related sheared rocks in the study area, based on our data and literature ones. The most common used aluminosilicate triple points are shown for reference: H71 = *Holdaway* [1971], P92 = *Pattison* [1992]. Mnz-in curves after *Kohn* [2016] and *Waizenhöfer and Massonne* [2017]. Aln + Chl-in curve after *Spear* [2010]. Temperature ranges of quartz microstructures after *Stipp et al.* [2002a, b] (see text for more details).
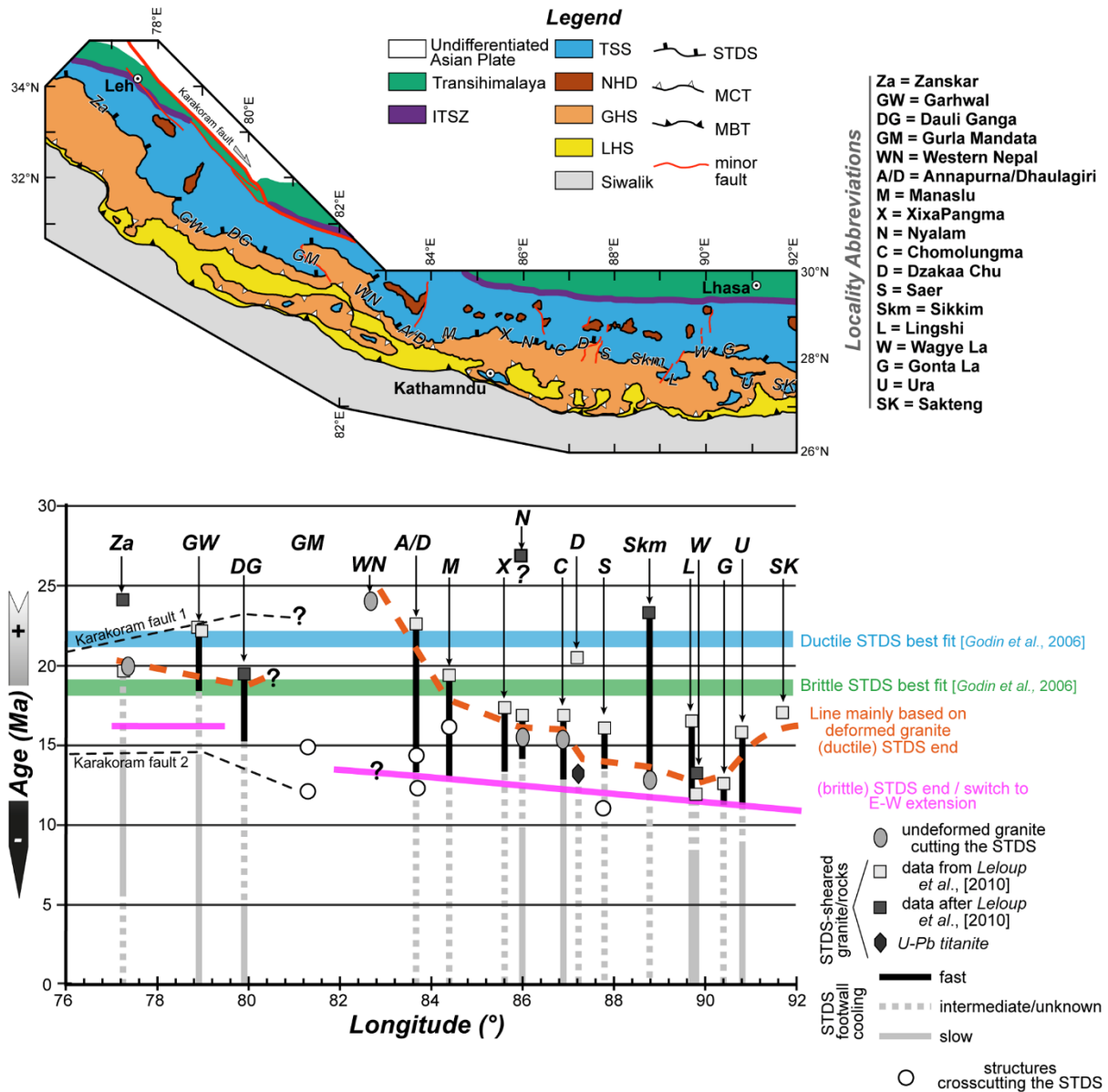
Figure 8. Summary of STDS deformation ages along the Himalaya modified after *Leloup et al*. [2010]. Original abbreviations for specific areas of *Leloup et al*. [2010] are maintained for consistency.